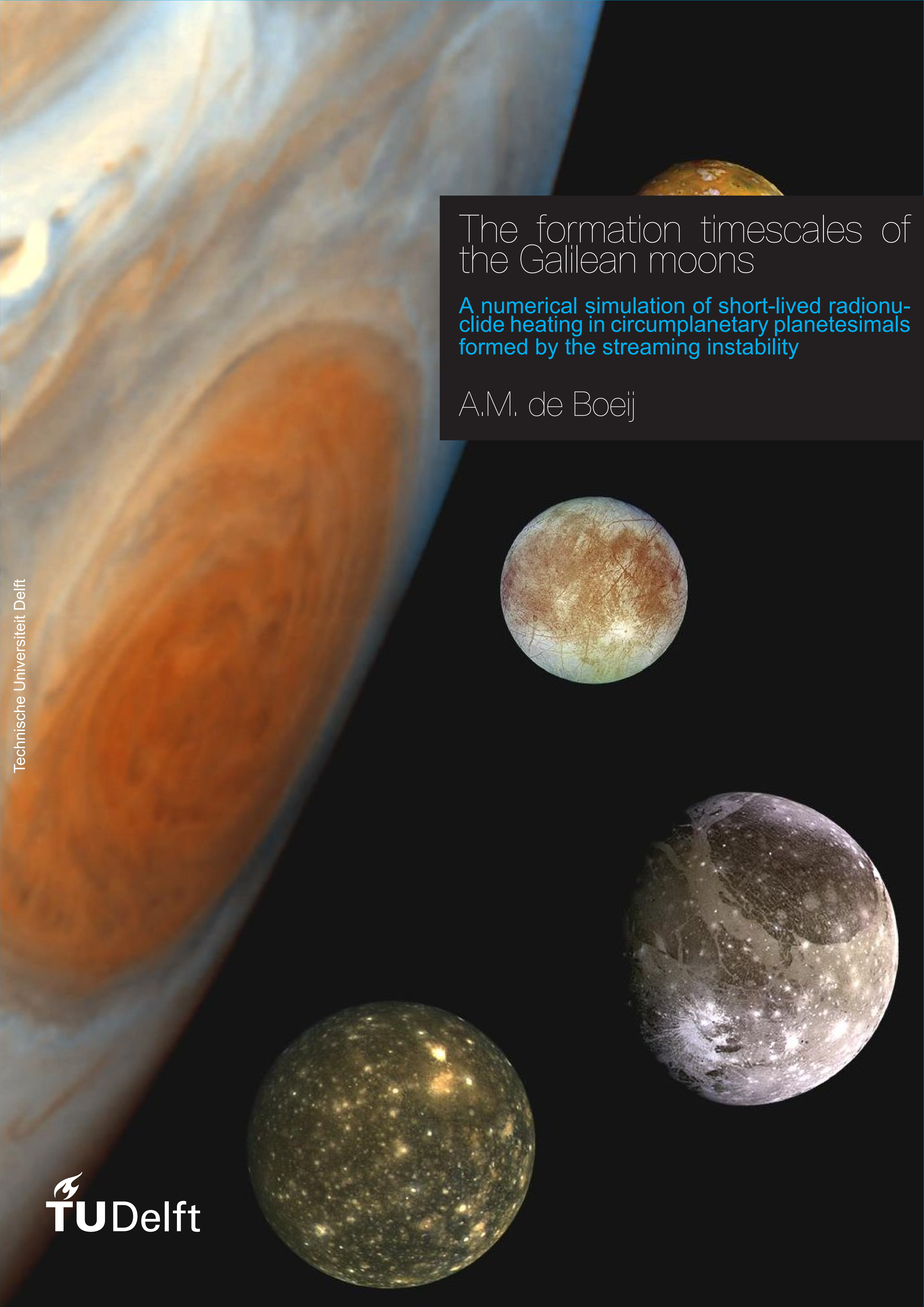

The formation timescales of the Galilean moons

A numerical simulation of short-lived radionuclide heating in circumplanetary planetesimals formed by the streaming instability

A.M. de Boeij

Technische Universiteit Delft

The formation timescales of the Galilean moons

A numerical simulation of short-lived radionuclide heating in circumplanetary planetesimals formed by the streaming instability

by

A.M. de Boeij

to obtain the degree of Master of Science
at the Delft University of Technology,
to be defended publicly on Friday May 13, 2022 at 10:00 AM

Student number:	4490142	
Project duration:	April 9, 2021 – May 13, 2022	
Thesis committee:	Prof. Dr. L.L.A. Vermeersen	TU Delft, committee chair
	Dr. A. Menicucci,	TU Delft, examiner
	Dr. S. Cazaux,	TU Delft, supervisor
	N. Oberg,	TU Delft, supervisor

Front cover image credits: NASA/JPL/DLR - NASA planetary photojournal, borders removed by Daniel Arnold NASA planetary photojournal, PIA00600
`http://photojournal.jpl.nasa.gov/jpeg/PIA00600.jpg`

Preface

This report will be the final chapter in my beautiful career at the TU Delft, and has only been made possible by the support of my supervisors and friends. After my positive experiences during your supervision of my Planetary Sciences II project, I did not hesitate to inform about possible thesis topics with Stephanie Cazaux as my supervisor. Thanks for your valuable time and positive feedback. I also can not stress enough how much the help of Nick Oberg helped me in the completion of this thesis. Your knowledge about this topic is seemingly endless, and your patience and support during our meetings is admirable.

Dear Grandpa, if there is anyone to whom I owe my interest in space, it is you. Having seen Jupiter and the Galilean moons through your telescope on Ameland when I was little to now performing research on their formation is no coincidence. I know you would have been so proud if you could have visited my thesis presentation, no matter what the result might have been, thank you. Dear mom and dad, thanks for listening to me on the phone and providing soothing advice whenever I needed it.

What started as a lonely thesis from home, luckily changed halfway during the project. Being able to talk with my fellow students again about our struggles during our thesis was more valuable than I previously imagined. So thanks to Pippa, Sybe, Stefan, Didier, Julia, Patrick, Sjoerd, Toon and Pieter for helping out but above all the endless lunches and walks around applied science faculty. Working from home has not always been easy with housemates like you, but coming home after a long day at the faculty and crashing on the couch together sure has been helpful. Thanks Roland, Jaime, Max ans Joram!

A.M. de Boeij
Delft, May 2022

Abstract

Context: The Galilean moons are expected to have formed in a circumplanetary disk (CPD) and exhibit a characteristic compositional gradient: an increasing ice mass fraction with increasing distance from Jupiter. Ice released from hydrated silicates formed inside planetesimals might be the cause of this compositional gradient. One of the mechanisms known to cause significant heat in the early solar system is radiogenic heating by ^{26}Al, so a different formation time for each Galilean moon could potentially explain a fully dehydrated Io, a low ice mass faction on Europa and $\sim 50\%$ ice mass fractions on Ganymede and Callisto.
Aims: We aim to determine the mass fraction of hydrated silicates of the planetesimals in Jupiter's CPD formed by radiogenic heating of ^{26}Al to constrain the formation times of the Galilean moons.
Methods: This is done using a numerical thermal evolution model capable of evolving planetesimals over time and altering the composition based on the internal temperature. Planetesimals are initiated with an ice mass fraction, temperature and ammonia ice concentration similar to the dust in the CPD. Their interior compositions alter by aqueous alteration, differentiation and dehydration.
Results: Hydration of rocks inside planetesimals does not occur for formation times later than 4 Myr after Ca-Al inclusion (CAI) formation, and a mass fraction of hydrous rocks of 73% is formed for 3 Myr after CAI formation. Larger planetesimals able that produce hydrated silicates dominate the compositional evolution of the population. A reduction in ammonia concentration in the ice by 50% increases the time needed to create hydrated silicates at 3 Myr after CAI formation from 1.5 Myr to > 2 Myr.
Conclusions: If Io formed before 4 Myr, it should have lost its ice no later than 1 Myr to prevent aqueous alteration. The low ice mass fraction on Europa could be explained by planetesimals formed at 3 Myr after CAI formation over a period of 1.5 Myr with a hydrous rock mass fraction of 66%, able to release 6.3% ice mass by dehydration. If the interior of Ganymede differentiated by radiogenic heating, the planetesimals should be formed before 4 Myr after CAI formation. Callisto's partially differentiated interior requires formation times of planetesimals after 4 Myr after CAI formation.

Contents

Nomenclature

Abbreviations and acronyms

A&A	Astronomy and Astrophysics
CAI	Ca-Al inclusions
CPD	Circumplanetary disk
JI	Jovian satellite I: Io
JII	Jovian satellite II: Europa
JII	Jovian satellite III: Ganymede
JIV	Jovian satellite IV: Callisto
JUICE	Jupiter Icy Moons Exporer
ProDiMo	Protoplanetary Disk Model
SI	Streaming Instability
SLRN	Short-lived radionuclides

Constants

σ	Stephan-Boltzmann constant	$5.670\,374\,419 \times 10^{-8}\,\mathrm{W\,m^{-2}\,K^{-4}}$
AU	Astronomical Unit	$1.495\,978\,71 \times 10^{11}\,\mathrm{m}$
G	Gravitational constant	$6.674\,30 \times 10^{-11}\,\mathrm{m^3\,kg^{-1}\,s^{-2}}$
R_j	Radius of Jupiter	$6.9911 \times 10^{7}\,\mathrm{m}$

Symbols

$(N/H)/(N/H)_{\odot}$	Nitrogen enrichment
$\bar{\kappa}$	Mean thermal diffusivity
$\bar{\rho}$	Mean density
$\bar{c}$	Mean specific heat
$\bar{K}$	Mean thermal conductivity
Δf_h	Hydrous rock lost due to dehydration reaction
Δf_i	Ice lost during ice melting
Δf_w	Water production during ice melting
ΔR	Numerical planetesimal layer thickness
Δt	Numerical time step
ΔT_m	Difference in melting temperature
ϵ	Mass fraction error

ϵ_m Aliasing error introduced by layer differentiation

κ Thermal diffusivity

λ Decay constant

$\lambda_{^{26}Al}$ Decay constant of ^{26}Al

$\lambda_{^{60}Fe}$ Decay constant of ^{60}Fe

ρ Density

ρ_p Planetesimal density

Σ_g CPD surface density

τ_I Timescale of type-I migration

τ_s Settling time of differentiation

τ_{acc} Duration of accretion

^{26}Al Radioactive isotope aluminium-26

^{27}Al Stable isotope aluminium-27

^{60}Fe Radioactive isotope iron-60

A Linear ammonia concentration parameter for the computation of melting temperature

a Cubic pressure parameter for the computation of melting temperature

$A_{^{26}Al}$ Radiogenic heat of ^{26}Al generated in rock

$A_{^{60}Fe}$ Radiogenic heat of ^{60}Fe generated in rock

B Cubic ammonia concentration parameter parameter for the computation of melting temperature

b Linear pressure parameter for the computation of melting temperature

C Shared pressure and ammonia concentration parameter for the computation of melting temperature

c Specific heat

C_1 SI computation parameter

d Radial distance to Jupiter

E_a Gravitational binding energy

$E_{^{26}Al}$ Decay energy of ^{26}Al

$E_{^{60}Fe}$ Decay energy of ^{60}Fe

f Mass fraction

$f_{^{26}Al}$ Fraction of radioisotope ^{26}Al to stable isotope 27Al

$f_{^{60}Fe}$ Fraction of radioisotope ^{60}Fe to its stable isotopes

f_{Al} Abundance of aluminium

H Dehydration heat

h Histogram bin settings

j Numerical planetesimal layer indicator

K Thermal conductivity

L Latent heat of water

M_0 Truncation mass

M_p Planetesimal mass

M_R Mass of the surface layer

$M_{\mathrm{p,min}}$ Minimal planetesimal mass

$m_{^{26}Al}$ Nucleus mass of ^{26}Al

$m_{^{60}Fe}$ Nucleus mass of ^{60}Fe

M_{tot} Total SI population mass

N Number of planetesimals

n_m Number of melted layers

p' Powerlaw coefficient for SI computations

P Pressure

P_{sub} Sublimation pressure

Q_R Energy in the surface layer

Q_{cond} Energy from conduction between layers

Q_{rad} Energy from surface radiation

$Q_{^{26}Al}$ Energy generated by ^{26}Al decay

R Radius

R_m Radius of all melted layers

R_p Planetesimal radius

R_r Radius of rocky core

R_{Hill} Hill radius

$R_{\mathrm{r,num}}$ Numerical radius of rocky core

$R_{\mathrm{r,real}}$ True radius of rocky core

R_{min} Minimum planetesimal radius

T_0 Initial temperature

T_j^n Temperature inside layer j for time instance n

$t_{1/2,^{26}Al}$ Half-life of ^{26}Al

$t_{1/2,^{60}Fe}$ Half-life of ^{60}Fe

$t_{\mathrm{dehydration,start}}$ Start time of the dehydration reaction

$t_{\mathrm{dehydration,stop}}$ End time of the dehydration reaction

$T_{\mathrm{dehydration}}$ Dehydration temperature

T_{dust} Midplane dust temperature

t_{end} End of formation after CAI formation

$t_{\mathrm{ice,start}}$ Start time of ice melting

$t_{\mathrm{ice,stop}}$ End time of ice melting

$T_{\mathrm{j=0,max}}$ Maximum core temperature

T_{melt} Melting temperature

t_{start} Start of formation after CAI formation

$X_{\mathrm{NH_3}}$ Ammonia mass concentration

$X_{\mathrm{NH_{3}}_0}$ Original ammonia concentration in the CPD

Composition subscripts

h Hydrous rock

i Ice

r Anhydrous rock

w Water

1 Introduction

The Galilean moons are four giant satellites orbiting Jupiter at low eccentricity and inclination, a feature of regular moons that also points towards them being formed in a circumplanetary disk (CPD) around Jupiter (Lunine and D. Stevenson 1982; Canup and Ward 2002). The Galilean moons developed a compositional gradient, and when using gravity and magnetic field data along with imaging and infrared observations the approximate ice mass fractions for the moons Io, Europa and both Ganymede and Callisto are 0%, ~5-8%, and $\sim 50\%$ respectively (Schubert, Anderson, et al. 2004; Ogihara and Ida 2012). The two categories of theories to explain the ice fractions currently observed are that the ice mass fractions are primordial and have not changed over time, whereas the other theories state that the initial ice fraction has altered over time. Mosqueira and Estrada 2003 claimed that the conditions in the disk were such that the inner moons formed containing the currently observed ice mass fractions, meaning their building block were already dehydrated. Others explain that the moons all formed in ice-rich environments and lost their ice over time due to various mechanisms (Canup and Ward 2009; Ronnet, Mousis, and Vernazza 2017).

If moon formation proceeded similarly to planet formation, they may have accreted from planetesimals that formed in the CPD. The formation of planetesimals can be described by the streaming instability (SI) theory, where solid particles are concentrated in satellite forming regions due to the gas drag experienced in the disk and collapse into planetesimals due to gravitational collapse (Youdin and Goodman 2005; Johansen et al. 2014). Planetesimals can serve as seeds for the formation of larger bodies such as the Galilean moons. Typical planetesimals that are produced by the SI have a radius of around 10-100 km (Simon et al. 2016). If the Galilean moons formed from planetesimals, the planetesimals can undergo interior evaluation prior to incorporation into the moons, potentially explaining the resulting composition of the forming Galilean moons. The planetesimal internal temperature is driven by heating sources such as accretional heating, radiogenic decay of short-lived radionuclide (SLRN), tidal heating and viscous heating and may increase above the melting temperature of ice, causing partial or full differentiation of ice and rock (Tobie et al. 2014). Furthermore, aqueous alteration could cause serpentinization of olivine-rich rocks and might have produced highly hydrated rocky cores (Castillo-Rogez and Lunine 2010). If a forming Galilean moon loses its primordial icy mantle, water in the form of hydrated silicates could remain in the hydrous cores formed by aqueous alteration and be released to the surface by dehydration. Hydration of silicates in the CPD could thus explain the low ice mass fraction of Europa (Kargel et al. 2000).

A major contributor to the thermal budgets of forming moons is the short-lived radionuclide ^{26}Al, which was first investigated by Urey 1955. Later work by Lichtenberg et al. 2019 has shown the drastic impact on dehydration of the planetesimals. Dehydration implies both the removal of hydrous compounds from silicates and the devolatilisation of icy bodies. When combining the dehydrating potential of the short-lived radionuclide ^{26}Al and the debated origin of the compositional gradient, conclusions can be drawn about the correlation between the two, and possible constraints for the processes of the formation can be formulated. The isotope ^{26}Al is not produced in the solar system itself but is seeded by external stellar winds or supernovae (Young 2014; Gounelle 2015). This means the concentration will not have been the same for every planetary system in the universe, and different planetary and/or lunar compositions could be observed in other systems with different initial concentrations of short-lived radionuclides.

The dispersal of the solar nebula is estimated based on paleomagnetic analysis to have occurred 3.8 Myr after the solar system formation (Wang et al. 2017). Studies of meteorite paleomagnetism have shown that the formation of Jupiter according to the core accretion assumption grew via runaway gas accretion between 3.46 to 3.94 Myr after the formation of the first solids in the solar system, Ca-Al inclusions (CAI) (Weiss and Bottke 2021). The Galilean moons are believed to have formed near the end of the accretion of Jupiter as gas inflow to the planet slowed in the post-runaway growth stage. The moons are the surviving generation with earlier generations of satellites being lost to collisions with Jupiter (Canup and Ward 2009). Io either has to be formed completely ice-free or lose its initial ice over time. Tidal heating is often mentioned as the main driver for this loss of ices, but efficiencies of ice loss would have to be highly energy efficient for tidal heating to prove as the only driving force behind the dehydration on Io (Bierson and Nimmo 2020; Bierson and Steinbrügge 2021). The composition of Europa is situated between the fully dehydrated Io and ~50% ice mass Ganymede and Callisto, therefore also pointing towards a different compositional evolution. During its formation, the disk temperature around Europa is expected to have been too warm for ices to accrete onto the forming satellite and in order to explain the small amounts of hydrous material, the ice line moved within the satellite's orbit allowing the accretion of hydrous material (Canup and Ward 2009). Another explanation is that the low ice mass fraction formed from dehydration of hydrous material that formed in planetesimals. The aqueous alteration of planetesimals forms hydrous silicates that can remain inside a forming moon even if all its ice is lost due to various mechanisms (Kargel et al. 2000). The two moons with the highest concentration of ice are limited in formation time and the duration of formation to prevent the melting of ices. For Callisto, the interior is expected to be partially differentiated which poses another limit on the temperatures reached during formation (Schubert, D. J. Stevenson, and Ellsworth 1981). For Callisto to avoid melting by radiogenic heating during its accretion its formation must have completed no earlier than ~2.6 to 3 Myr after CAI formation (McKinnon 2006). Adding accretional heating extends this end of formation to 4 Myr after CAI formation (Barr and Canup 2008).

The reason that the compositional gradient of the Galilean moons is of interest to researchers, is because the moons are characterised by their co-planar, low inclination/eccentricity and prograde orbits and thus show resemblance to a planetary system. The six inner planets with a relatively similar radius of the TRAPPIST-1 system share a satellite/parent body ratio, potentially implying a similar formation history (Gillon et al. 2017). By understanding the dehydration effects of short-lived radionuclides on these satellite forming regions, assumptions about newly discovered exoplanets can be made regarding their ice fraction, taking into account that the fraction of ^{26}Al can be different from the one in the solar system. This could lead to a majority of icy planets or completely dehydrated planets.

1.1. Research questions

Following the theory discussed above, a research question has been formulated:

When did the Galilean moons form based on short-lived radionuclide heating?

Alongside the research question, several sub-questions have been formulated:

1. How does the total and individual composition of a population of planetesimals change when subjected to internal radiogenic heating?
   (a) What are the driving parameters for compositional changes due to radiogenic heating?
   (b) To what extent does ammonia ice affect the compositional changes?
   (c) Is there a preferred environment for the creation of hydrous rocks in planetesimals?
2. What are the constraints concerning the formation of the Galilean moons assuming their ice mass fraction was lost by radiogenic heating?
   (a) At what formation time does ^{26}Al not contribute to the production of hydrous rocks.
   (b) What locations in the CPD around Jupiter can be (de)hydrated by the effects of ^{26}Al.
   (c) How long do planetesimals need to survive in the CPD in order for aqueous alteration and differentiation to occur?

1.2. Report outline

This thesis will be presented in the form of a journal article and is shown in chapter 2. Verification and validation methods of the computations in the journal article are given in chapter 3. Conclusions and recommendations will be shown in chapter 4

2 Journal article

The bulk of this thesis has been documented in the form of a journal article, which will be presented in this chapter. The template chosen for this was taken from the journal Astronomy and Astrophysics (A&A).

The formation timescales of the Galilean moons

A numerical simulation of short-lived radionuclide heating in circumplanetary planetesimals formed by the streaming instability

A.M. de Boeij[1], N. Oberg[1,2], and S. Cazaux[1,3]

[1] Faculty of Aerospace Engineering, Delft University of Technology, Delft, The Netherlands
[2] Kapteyn Astronomical Institute, University of Groningen, P.O. Box 800, 9700 AV Groningen, The Netherlands
[3] University of Leiden, P.O. Box 9513, 2300 RA Leiden, The Netherlands

April 28, 2022

ABSTRACT

Context. The Galilean moons are believed to have formed in a circumplanetary disk (CPD). It is still unknown why the composition of the moons becomes increasingly icier with increasing distance from Jupiter. Ice released from hydrated silicates formed inside planetesimals might be the cause of the compositional gradient of the Galilean moons. Decay of the short-lived radionuclide (SLRN) over time reduces the radiogenic heat in planetesimals meaning less compositional alterations occur for late formation times. Different formation times for each Galilean moon could potentially explain a fully dehydrated Io, a low ice mass faction on Europa and ~ 50% ice mass fractions on Ganymede and Callisto.
Aims. We aim to determine the mass fraction of hydrated silicates of the planetesimals in Jupiter's CPD formed by radiogenic heating of ^{26}Al to constrain the formation times of the Galilean moons.
Methods. We produce a population of planetesimals based on the assumption that they form by the streaming instability mechanism. The formed planetesimals are analysed by a thermal interior evolution model using radiogenic heating and surface radiation. Planetesimals are initiated with an ice mass fraction, temperature and ammonia ice concentration similar to the dust in the CPD. Their interior compositions alter by aqueous alteration, differentiation and dehydration.
Results. Large planetesimals that show differentiation and hydration of silicates dominate the compositional evolution of the population. No hydrous rocks are formed for late formation times of 4 Myr after Ca-Al inclusion (CAI) formation, increasing to a weighted average hydrous rock mass fraction inside the CPD of 73% for formation of 3 Myr after CAI formation. A reduction in ammonia by 50% increases the time needed to create hydrated silicates at 3 Myr after CAI formation from 1.5 Myr to > 2.0 Myr.
Conclusions. Our findings suggest that Io and Europa should have formed before 4 Myr after CAI formation and have lost its ice no later than 1 Myr to prevent aqueous alteration. After 1.5 Myr the mass fraction of hydrated silicates is 66%, able to dehydrate and create a 6.3% ice mass Europa. If the interior of Ganymede differentiated by radiogenic heating, the planetesimals should be formed before 4 Myr after CAI formation. Callisto's partially differentiated interior requires formation times of planetesimals after 4 Myr after CAI formation.

Key words. Galilean moons – Short-lived radionuclides – Satellite formation

1. Introduction

Jupiter has four large regular moons that are expected to have formed in a CPD (Lunine & Stevenson 1982; Canup & Ward 2002; Mosqueira & Estrada 2003). These Galilean moons exhibit a radial compositional gradient, becoming increasingly icy with increasing distance from Jupiter. Their ice mass fractions have been given in Table 1. The origin of this compositional gradient is not fully understood. The currently observed ice mass fractions are either primordial or have developed over time by (de)hydration. Europa is different with respect to the other three moons since it is situated between the fully dehydrated Io and the ~50% ice by mass Ganymede and Callisto. The low ice mass fraction on Io and Europa were taken as evidence of their formation in hot regions of the CPD, largely inside the ice-line where water exists as ice (Lunine & Stevenson 1982). The ~5-8% ice content of Europa could have accreted during the final stages of its formation if the CPD cooled and the water ice-line swept inwards across the satellite's orbit (Canup & Ward 2009). Alternatively, Io and Europa may initially have been as icy as Ganymede and Callisto, but lost their ice to hydrodynamic escape (Bierson & Nimmo 2020). Other mechanisms that induce ice loss might have been giant impacts during formation (Dwyer et al. 2013) and tidal heating (Hay et al. 2020), the latter requiring extreme efficient ice loss to cause composition changes (Bierson & Steinbrügge 2021).

The Galilean moons are believed to have formed near the end of the accretion of Jupiter as gas inflow to the planet slowed in the post-runaway growth stage. The moons are the surviving generation with earlier generations of satellites being lost to collisions with Jupiter (Canup & Ward 2009). The dispersal of the solar nebula is estimated based on paleomagnetic analysis to have occurred ~3.8 Myr after the solar system formation (Wang et al. 2017). Studies of meteorite paleomagnetism have shown that the formation of Jupiter according to the core accretion assumption grew via runaway gas accretion between 3.46 to 3.94 Myr after the formation of the first solids in the solar system, Ca-Al inclusions (CAI) (Weiss & Bottke 2021). For Callisto to avoid melting by radiogenic heating during its accretion its formation must have completed no earlier than ~2.6 to 3 Myr

Table 1. Characteristics of the Galilean moons, with the distance from Jupiter d expressed in R_J, the radius of Jupiter. R is the radius of the moons (Schubert et al. 2004; Ogihara & Ida 2012).

Moon	**d** [R_j]	**R** [km]	**Ice fraction**
Io	5.9	1822	0
Europa	9.4	1565	5-8%
Ganymede	15.0	2631	45%
Callisto	26.4	2410	56 %

after CAI formation (McKinnon 2006). Adding accretional heating extends this end of formation to 4 Myr after CAI formation (Barr & Canup 2008).

If moon formation proceeded similarly to planet formation, they may have accreted from planetesimals that formed in the CPD. The formation of planetesimals can be described by the streaming instability (SI) theory, where solid particles are concentrated in satellite forming regions due to the gas drag experienced in the disk and collapse into planetesimals due to gravitational collapse (Youdin & Goodman 2005; Johansen et al. 2014). Planetesimals can serve as seeds for the formation of larger bodies such as the Galilean moons. Typical planetesimals that are produced by the SI have a radius of around 10-100 km (Simon et al. 2016). If the Galilean moons formed from planetesimals, the planetesimals can undergo interior evaluation prior to incorporation into the moons, potentially explaining the resulting composition of the forming Galilean moons. The planetesimal internal temperature is driven by heating sources such as accretional heating, radiogenic decay of short-lived radionuclide (SLRN), tidal heating and viscous heating and may increase above the melting temperature of ice, causing partial or full differentiation of ice and rock (Tobie et al. 2014). Furthermore, aqueous alteration could cause serpentinization of olivine-rich rocks and might have produced highly hydrated rocky cores (Castillo-Rogez & Lunine 2010). If a forming Galilean moon loses its primordial icy mantle, water in the form of hydrated silicates could remain in the hydrous cores formed by aqueous alteration and be released to the surface by dehydration. Hydration of silicates in the CPD could thus explain the low ice mass fraction of Europa (Kargel et al. 2000). The presence of ammonia alters the melting curves of ices (Leliwa-Kopystyński et al. 2002). Ammonia-containing planetesimals are expected between 5-10 au given the high nitrogen enrichment in Jupiter (N/H)/(N/H)$_\odot$ = 3.3 (Owen & Encrenaz 2003), and outer solar circumstellar-disk modelling suggests the ammonia fraction relative to water NH_3/H_2O is 14% (Dodson-Robinson et al. 2009).

Work by Lichtenberg et al. (2019) has shown that the decay heat from the SLRN ^{26}Al is able to power the interior evolution of planetesimals in the early solar system by causing silicate melting and degassing of primordial water abundances (Monteux et al. 2018). If the half-life of a SLRN is comparable to the formation time of satellites inside a CPD, its heating potential is much lower at the end of formation compared to the initial start of formation. The most potent SLRN in the early solar system is ^{26}Al, with a half-life $t_{1/2,^{26}Al}$ of 0.717 Myr (Norris et al. 1983). The fraction of the radio-isotope over its stable component $^{26}Al/^{27}Al$ during CAI formation is $5.23{\pm}0.13{\times}10^{-5}$ (Jacobsen et al. 2008; Davis et al. 2014). Besides ^{26}Al, the most potent SLRN is ^{60}Fe. A rough estimate on the heat production between ^{26}Al and ^{60}Fe in section B.1 shows ^{60}Fe only becomes dominant over ^{26}Al at 12.6 Myr after CAI formation, potentially after the stage of Galilean moon formation. Planetesimals formed in a CPD around Jupiter would have formed much later compared to the ones formed in the circumstellar disk. A difference in formation time could alter the heating potential of ^{26}Al, leading to either the absence, melting or preservation of initial ices in forming planetesimals. Even in the late stage of > 3 Myr as expected for Jupiter's formation, could ^{26}Al still play a large role in composition alterations and the hydration of silicates by aqueous alteration?

In this work, we aim to determine the formation times of the Galilean moons by:

1. Modelling planetesimal population
2. Modelling thermal evolution of that population:
   - for different ^{26}Al concentrations (formation times)
   - for different ammonia ice fractions
3. Studying resulting planetesimal composition
4. Seeing for what formation time and after how much time hydration of silicates and differentiation occurs that could explain the composition of the Galilean moons

The numerical method of both the planetesimal population generation and the thermal evolution model along with chosen variables are described in section 2. In section 3 the results are presented, followed by a discussion of the obtained results where they are analysed and tied to the formation of the Galilean moons is section 4. A conclusion is presented in section 5.

2. Numerical model

The numerical model is based on the following mechanisms and assumptions:

1. The properties of dust in the CPD are determined using a thermochemical disk model.
2. A planetesimal population forms instantaneously within the CPD via streaming instability and does not accrete any material after formation.
3. Planetesimal interiors are initially homogeneous and have a similar temperature, ice mass fraction and ammonia ice concentration relative to the dust in the CPD.
4. Planetesimals undergo interior thermal evolution based on radiogenic heating and surface radiation causing aqueous alteration, differentiation and dehydration.
5. Planetesimals remain in the CPD and survive against migration/gas drag.

The interior thermal evolution of the planetesimals is modelled using the numerical method of Wakita & Sekiya (2011), updating the composition of each planetesimal according to the obtained temperatures. This work also builds upon the existing thermal model to include the processes of refreezing, realistic radiative surface cooling and ammonia ice. If the planetesimals formed instantaneously, their gravitational binding energy per unit mass $E_a \sim (GM_p/R_p)$, taken as a reference for energy from accretion is $E_a \sim 3.6 \times 10^4$ J kg^{-1} for the largest planetesimal with R_p = 400 km. This is smaller than the latent heat of water ($3{\times}10^5$ J kg^{-1}) and raises the temperature by approximately 40 K (Barr & Canup 2008). No melting would thus occur given planetesimals are assumed to accrete instantaneously and retain all their accretional energy. Since migration is not taken into account, a planetesimal formed with certain CPD conditions remains in place during the entire thermal evolution. Taking again the largest planetesimals with $R_p \sim 400$ km, type-I migration timescales are expected of $\tau_I > 10^6$ Myr for a surface density of $\Sigma_g \sim 400$ g cm^{-1}, the largest gas surface densities observed in the CPD (Tanaka et al. 2002; Canup & Ward 2009).

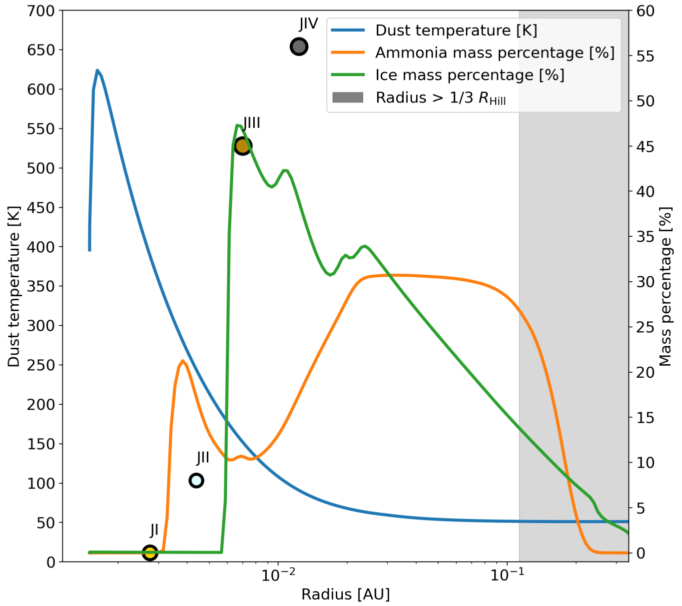

Fig. 1. Radial circumplanetary midplane properties derived from thermochemical disk model (Appendix A), dust temperature (blue) ice mass fraction (green) and ammonia concentration (orange). The radial position and the ice mass fraction of the four Galilean moons Io (JI), Europa (JII), Ganymede (JIII) and Callisto (JIV) are indicated by the coloured circles. The unstable region of the CPD outside 1/3 $R_{\rm Hill}$ is highlighted in grey.

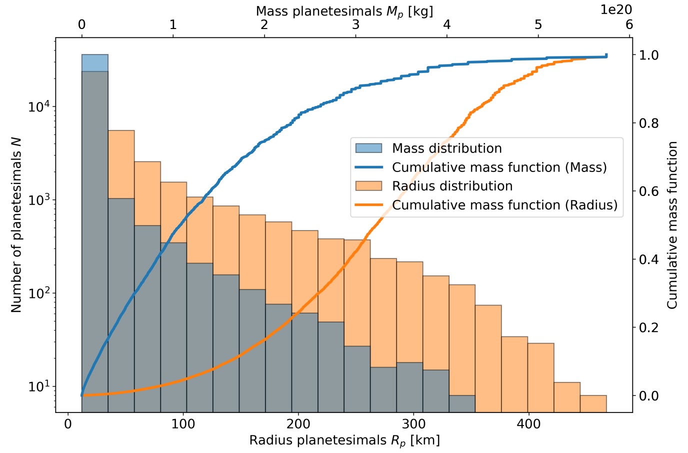

Fig. 2. Mass (blue) and radius (orange) distribution of the sampled planetesimal population. The cumulative mass function for both distributions are given in their respective colours.

2.1. Ambient conditions in the CPD Midplane

The radial profile of a CPD around Jupiter inside a gap in the circumstellar disk provides the initial compositional and ambient properties of the CPD dust and gas used in the thermal- and compositional evolution of section 2.3 for the planetesimal population from section 2.2. An explanation of the disk modelling code can be found in Appendix A. The radial profile provides the ice mass fraction of the dust f_i and the ammonia concentration inside this ice $X_{\rm NH_3}$ in percentage and midplane temperature $T_{\rm dust}$ in K for given radial positions a in au, which provides input parameters to the thermal evolution of the planetesimals. Both the initial planetesimal and the background thermal temperature are equal to $T_{\rm dust}$, since the gas and dust temperatures do not deviate more than 0.5% in the optically thick regions of the CPD. The relevant properties of the CPD midplane are shown in Figure 1. The CPD is unstable and truncated around 1/3 of the companion's Hill radius $R_{\rm Hill}$, shown in the grey region (Martin & Lubow 2011; Shabram & Boley 2013). The temperature can be seen to have a peak of 624 K decreasing to a minimum value of 51.2 K due to the background radiative heating in the circumstellar gap, which is in line with the expected approximate background temperature of the dust in the circumstellar gap (Oberg et al. 2020). The ice mass fraction of the dust becomes significant from a radius of 5.88 $\times10^{-3}$ au onward, reaching a maximum value of 47.3%. The ammonia concentration peaks at 30.7%, showing relatively lower values around the peak of the ice mass fraction. This work focuses on locations in the CPD where the ice mass fraction is non-zero, given it is required to perform aqueous alterations. We assume all rocks are initially anhydrous and also consider variations of the radial ammonia ice mass fraction, scaling the original ammonia concentration $X_{\rm NH_{30}}$ by 100%, 50% and 0%.

2.2. Streaming instability planetesimals

Abod et al. (2019) showed using numerical simulations of streaming instability in a CPD characterised by its pressure gradient and the balance between self-gravity and shear that the cumulative planetesimal population distribution $N(>M_p)$ as a function of planetesimal mass M_p can be described by an exponentially truncated power-law given in Equation 1 with parameter C_1 given in Equation 2.

$$N(>M_p) = C_1 M_p^{-p'+1} e^{M_{p,min}/M_0} \tag{1}$$

$$C_1 = n M_{p,min}^{p'-1} e^{M_{p,min}/M_0} \tag{2}$$

In the above equation, p' is the power-law coefficient determined by literature, $M_{\rm p,min}$ the minimum planetesimal mass in the population in kg, M_0 the truncation mass in kg and n the number of planetesimals generated. The truncation mass M_0 varies for different locations inside the CPD based on the surface density Σ_p and the orbital frequency Ω and is of the order 10^{20} kg at the location of the ice-line (radius = 0.006 au). Sampling from this cumulative distribution is done by taking the probabilities from the theoretical distribution with a resolution linked to the number of bins h from which planetesimals can be sampled until desired disk mass $M_{\rm tot}$ is reached. A total mass of 3.2×10^{23} kg is chosen, equal to the total mass of the satellitesimal population used in the work of Batygin & Morbidelli (2020). Using the variables from Table 2, 38093 planetesimals are generated and shown in Figure 2. Due to the power-law distribution, smaller bodies dominate the number density of the population. According to the cumulative mass function, it can be seen that 50% of the mass is accounted for by all bodies with a mass larger than 1.04×10^{20} kg. This computes to a planetesimal with R_p 265 km when assuming an ice mass fraction $f_i = 0.623$ ($\bar{\rho} = 1345$), ratios of Si : Fe : Mg = 1 : 1 : 1 given by the approximate ratios of the solar abundance and the mineral inside the rock to be olivine ($(Mg_{0.5}, Fe_{0.5})_2SiO_4$) (Wakita & Sekiya 2011).

Instead of determining the interior evolution of every individual planetesimal within the population, the population is represented as 5 individual planetesimals with their number of occurrence shown in Table 3. The associated numerical error of representing 38093 planetesimals with 5 individual radii is discussed in section C.1. The total mass fraction for different com-

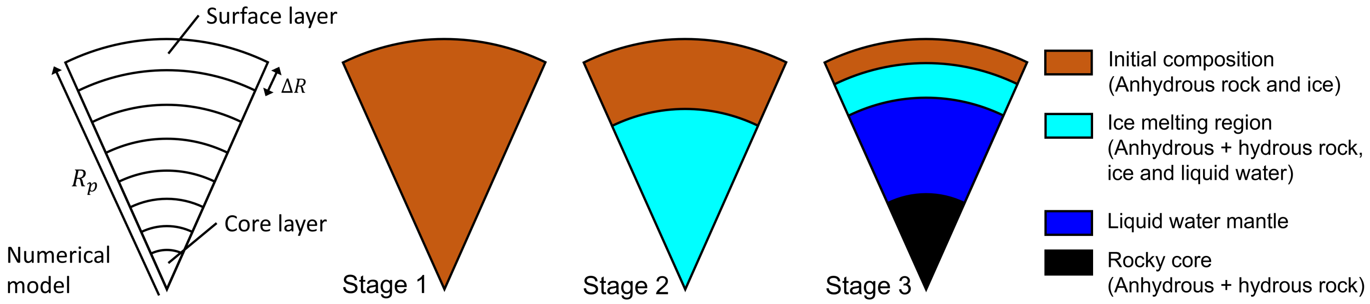

Fig. 3. Schematic representation of the numerical thermal evolution model and the different stages of icy planetesimal interior evolution. The planetesimal with radius R_p is divided in layers of constant width ΔR. Initially, the planetesimal begins as being composed primarily of an anhydrous rock and ice mixture. increased temperature causes ice to melt in stage 2. Stage 3 shows the separation of a rocky core and a liquid water mantle, with the initial composition and ice melting regions on top.

Table 2. Variables used for planetesimal population distribution sampling and Equation 1 and 2 (Abod et al. 2019; Batygin & Morbidelli 2020).

Sym	Parameter	Value	Unit
p'	Power-law coefficient	1.3	-
$R_{\min}$	Minimum radius	10^5	m
M_0	Truncation mass	10^{20}	kg
M_{tot}	Total population mass	3.2×10^{23}	kg
h	Sampling histograms	10^5	-
ρ_p	Planetesimal density	1345	kg m^{-3}

Table 3. Planetesimal population from Figure 2 classified into five categories based on size.

Planetesimal radius R_p [km]	Number of bodies
12	33391
103	3198
194	1456
285	566
376	82

positions is determined by multiplying the individual planetesimal composition with its occurrence.

2.3. Thermal evolution

The numerical time integration is performed using an explicit method defined by Wakita & Sekiya (2011), developed to analyse the thermal evolution of icy planetesimals in the solar nebula using a finite difference method where the planetesimal radius R_p is divided in layers of constant layer thickness ΔR. A schematic representation of the planetesimal used in this numerical integration is given in Figure 3. It is clear that the planetesimal is divided into separate layers with thickness ΔR. For each layer inside the planetesimal, the temperature at the following time step Δt is computed, altering the composition and thermal properties accordingly. The layers are thermally affected by internal radiogenic heating of ^{26}Al of and via conduction of their neighbouring layers. The core and surface layers are treated separately since they have only one neighbouring layer. The temperature T_j^n in K inside a layer j for time n is numerically integrated over time Δt to T_j^{n+1}. For non-core and surface layers where $j \neq 0$ and $j \neq R/\Delta R - 1$, Equation 3 is used. The thermal evolution of the surface layer ($j = R_p/\Delta R - 1$) is discussed in section 2.3.2.

$$T_j^{n+1} = T_j^n + \frac{\kappa\Delta t}{j\Delta r^2}\left((j+1)T_{j+1}^n - 2jT_j^n + (j-1)T_{j-1}^n\right) + \kappa\Delta t\frac{A_{^{26}Al}}{K}e^{(-\lambda t^n)} \tag{3}$$

The core temperature T_0^{n+1} where $j = 0$, Equation 4 applies.

$$T_0^{n+1} = T_0^n + \frac{6\kappa\Delta t}{\Delta r^2}\left(T_1^n - T_0^n\right) + \kappa\Delta t\frac{A}{K}\exp(-\lambda t^n) \tag{4}$$

In the above equations, T_j^n denotes the temperature in K at time n in layer j, K is the thermal conductivity in W kg^{-1} K^{-1}, t is the time after CAI formation and λ is the decay constant for the short-lived radionuclide. Furthermore, κ is the thermal diffusivity in m^2 s^{-1} and is computed in Equation 9. Finally, $A_{^{26}Al}$ is the radiogenic heat computed according to Equation 5 in W m^{-3}.

$$A_{^{26}Al} = \left(\frac{E_{^{26}Al}\lambda_{^{26}Al}f_{Al}f_{^{26}Al}}{m_{^{26}Al}}\right)\bar{\rho}f_r \tag{5}$$

The first part of the equation computes the decay energy of ^{26}Al in a kg of rock, with the second term computing the amount of rock inside a layer of the planetesimal according to the rock mass fraction and its mean density. Note the difference between the fraction of aluminium f_{Al} inside rocky material and the isotope fraction of ^{26}Al over ^{27}Al $f_{^{26}Al}$. The bar symbol in $\bar{\rho}$ indicates the mean density and f_r is the mass fraction of rock. The other parameters for ^{26}Al can be found in Table 4. Computing the mean value of density $\bar{\rho}$ along with the specific heat $\bar{c}$ and thermal

Table 4. Constants of short-lived radionuclide ^{26}Al.

Sym	Parameter	Value	Unit	Source
f_{Al}	Al Abundance	8.37×10^{-3}	-	(1)
$f_{^{26}Al}$	^{26}Al Abundance	5.0×10^{-5}	-	(1)
$\lambda_{^{26}Al}$	Decay constant	9.63×10^{-7}	yr^{-1}	(2)
$E_{^{26}Al}$	Decay energy	3.16	MeV	(3)
$m_{^{26}Al}$	Nucleus mass	25.98689186	u	(4)

References. (1) Lodders (2019); (2) Jacobsen et al. (2008); (3) Schramm & Wasserburg (1970); (4) Huang et al. (2017).

Table 5. Material properties of rock, water and ice used in Wakita & Sekiya (2011).

Sym	Parameter	Unit	Rock	Ice	Water
ρ	Density	kg m^{-3}	3300	1000	1000
c	Specific heat	J kg^{-1} K^{-1}	910	1900	4200
K	Conductivity	W m^{-1} K^{-1}	3.0	2.2	0.56

conductivity $\bar{K}$ is done by Equation 6, 7 and 8 respectively.

$$\bar{\rho} = \left(\frac{fr}{\rho_r} + \frac{f_i}{\rho_r} + \frac{f_w}{\rho_w}\right)^{-1} \tag{6}$$

$$\bar{c} = f_r c_r + f_i c_i + f_w c_w \tag{7}$$

$$\bar{K} = \bar{\rho}\left(\frac{f_r K_r}{\rho_r} + \frac{f_i K_i}{\rho_i} + \frac{f_w K_w}{\rho_w}\right) \tag{8}$$

$$\kappa = \frac{K}{\rho c} \tag{9}$$

Subscripts r,i and w indicate rock, ice and water respectively, and their material properties can be found in Table 5, where the densities of ice and water are assumed to be equal (Yomogida & Matsui 1983; Murphy & Koop 2005; *Chronological Scientific Tables* 2010).

2.3.1. Interior composition evolution

The initial composition of the planetesimals formed by this model is assumed to be a mixture of olivine and water ice (including ammonia, see section 2.3.2). During the thermal evolution of a planetesimal, the composition in a specific layer is altered based on its temperature and thermal characteristics. The different phases in the interior of the planetesimal are described in the following sections. The first phase transition occurs when the melting temperature of ice is reached and changes anhydrous rocks into hydrous rocks. The second transition occurs at a similar temperature and transforms any remaining ice into liquid water and the third is concerned with the differentiation of a rocky core and a liquid water mantle. The last transition dehydrates the hydrous rocks once the dehydration temperature is reached. The combination of these phase transitions in each layer leads to different stages in the total composition of the planetesimals shown in Figure 3, with an initial state defined as stage 1. For stage 2, several core layers have already reached the melting temperature of ice, initiating the aqueous alteration reaction followed by the melting of the remaining ice. If the ice content of a layer is completely melted, the rocks sink to the core leaving a liquid water mantle in between the formed rocky core and the initial composition- and ice melting layers.

Aqueous Alteration

Once the melting temperature of ice inside a layer is reached, the aqueous alteration reaction is assumed to occur instantaneously and anhydrous rocks together with liquid water form hydrous rocks. This process is shown in Equation 10 (Tomeoka & Buseck 1988). The terms in this equation from left to right correspond to the molecular formulae of olivine, water, serpentine, saponite, and magnetite.

$$\begin{aligned}
&(\mathrm{Mg}_{0.5}, \mathrm{Fe}_{0.5})_2\mathrm{SiO}_4 + \mathrm{H}_2\mathrm{O}\ (aq) \\
&\quad = 1/3\ (\mathrm{Mg}_{0.8}, \mathrm{Fe}_{0.2})_3\mathrm{Si}_2\mathrm{O}_5(\mathrm{OH})_4 \\
&\quad +1/12\ (\mathrm{Mg}_{0.8}, \mathrm{Fe}_{0.2})_3\mathrm{Si}_4\mathrm{O}_{10}(\mathrm{OH})_2 \\
&\quad +1/4\ \mathrm{Fe}_3\mathrm{O}_4 + 1/4\ \mathrm{H}_2
\end{aligned} \tag{10}$$

Based on the molecular weights of Equation 10 the mass fraction changes based on this chemical formula are given in Equation 11, 12 and 13 where f_h and f_w are the hydrous rock and liquid water mass fractions. For $f_i = 0.095$, all initial anhydrous rock and ice is converted into hydrous rock, meaning excess ice remains for $f_i > 0.095$ and not all rocks can be hydrated for $f_i < 0.095$. The density of the hydrous rock is lower compared to the original anhydrous rock due to the incorporation of water and computes to $\rho_h = 2709.7$ kg m^{-3}.

$$f_h = 1.104628 \cdot f_r \tag{11}$$

$$f_i = 1 - 1.904628 \cdot f_r \tag{12}$$

$$f_w = 0.8 \cdot f_r \tag{13}$$

Ice melting

Once a layer has finished the aqueous alteration in which ice and anhydrous rocks are converted to hydrous rocks for $f_i > 0.095$, excess ice remains inside the aqueous altered layer. The remaining ice start melting, and the changing mass fractions of liquid water Δf_w and ice Δf_i are computed by Equation 14 using the latent heat of water $L = 3.34 \times 10^5$ J kg^{-1} (Legates 2005).

$$\Delta f_w = -\Delta f_i = \bar{c}(T_j^n - T_{\mathrm{melt}})/L \tag{14}$$

During these compositional changes, the temperature in the melting layer is kept constant at a value of T_{melt} thus assuming that all temperature increases power the phase change of ice to liquid water. Changes according to Equation 14 continue until $f_i < 0$, at which point the ice mass fraction is set to zero and the liquid water fraction equals $f_w = 1 - f_h - f_r$.

Layer differentiation

For simplicity, the separation of the liquid water and rock layers is assumed to happen at the exact moment of total melting of the ice, given the settling time τ_s for 1 mm size rocks is of order 10^6 s and the thermal evolution of the order of 1 Myr. Wakita & Sekiya (2011) At every time step Δt the number of layers that have finished melting n_m (all layers where $f_i = 0$) sink down and the separation boundary radius for rock R_r in km is given in Equation 15, where R_m is the radius of all melted layers, obtained following $R_m = n_m \Delta R$. The liquid water mantle originates from R_r and continues up to R_m

$$R_r = (f_r R_m^3 \frac{\bar{\rho}}{\rho_r})^{1/3} \tag{15}$$

$$\epsilon_m = \frac{4}{3}\pi((\rho_W - \rho_R)(R_{r,num}^3 - R_{r,real}^3)) \tag{16}$$

This does introduce an aliasing error since R_r is not necessarily a multiple of ΔR. The numerical boundary $R_{\mathrm{r,num}}$ has an error of at most $0.5\Delta R$ from the true separation boundary $R_{\mathrm{r,real}}$. The maximum mass error ϵ_m in kg with respect to the original planetesimal can be computed using Equation 16. The planetesimal mass thus varies, increasing for $R_{\mathrm{r,num}} > R_{\mathrm{r,real}}$ and vice versa. This effect increases for larger n_m, R_p and ΔR since the mass per layer increases for larger radii. This error also decreases when more hydrous rock is present in the core since it has a density closer to water compared to anhydrous rock. The effect of ϵ_m is shown in section C.3.

The newly formed liquid water mantle is at temperature T_{melt}, assuming all heat from the rocky core penetrates through the liquid water mantle which remains in thermal equilibrium thus assuming perfectly efficient convection. Allowing the rocky core to interact with the surface makes sure the liquid water mantle does not act as an insulator for the heat of the rocky core, limiting the heating of surface material and ultimately less hydrous rock production.

Dehydration reaction

The hydrous rocks that formed in the aqueous alteration will lose their water content via the dehydration reaction according to Equation 17 when a layer reaches a temperature of 873 K (Nozaki et al. 2006). The mineral composition is taken from Tomeoka & Buseck (1988), assuming that the iron ratio of dehydrated olivine is similar to the serpentine and saponite (Wakita & Sekiya 2011).

$$\begin{aligned}&1/3\ (\mathrm{Mg_{0.8}}, \mathrm{Fe_{0.2}})_3\mathrm{Si_2O_5(OH)_4}\\ &\quad +1/12\ (\mathrm{Mg_{0.8}}, \mathrm{Fe_{0.2}})_3\mathrm{Si_4O_{10}(OH)_2}\\ &\quad = 5/8(\mathrm{Mg_{0.8}}, \mathrm{Fe_{0.2}})_2\mathrm{SiO_4} + 3/4\ \mathrm{H_2O} + 3/8\ \mathrm{SiO_2}\end{aligned} \tag{17}$$

It can be seen that the hydrated serpentine and saponite form dehydrated olivine, silica and water. The magnetite that is formed from the aqueous alteration remains. The densities of the remaining rocky compounds are again equal to ρ_r. The alteration of hydrous mass fraction Δf_h is computed using Equation 18.

$$\Delta f_h = -c_r(T_j^n - T_d)/H \tag{18}$$

In the above equation, c_r is the specific heat of anhydrous rock (see Table 5), $T_{\mathrm{dehydrate}}$ the dehydration temperature in K and H the endothermic heat for the dehydration reaction equal to 4.17×10^5 J kg^{-1}. Currently, the liquid water released inside a layer during the dehydration reaction in the core does not differentiate upward into the liquid water mantle. This process is repeated until the mass fraction of the hydrated rock reaches 0.3, which is the point where all serpentine and saponite have formed olivine and silica. The remaining 0.3 is the remaining anhydrous magnetite.

2.3.2. Additions to the thermal evolution model

We have expanded upon the thermal evolution model of Wakita & Sekiya (2011) by including radiative cooling on the surface, refreezing of the liquid water mantle, and the presence of ammonia and its effect on reducing the ice melting temperature. The addition of surface radiative cooling allows the surface temperature to increase above the ambient background increasing temperatures in the sub-surface layers. Sublimation and outgassing are not modelled in this work but their potential is explored given the current surface radiation assumptions. With added refreezing of the liquid water mantle, the first layer at constant temperature T_{melt} can decrease its temperature normally once all liquids have frozen back to ice. This would ultimately allow the rocky core to cool down, potentially lowering the maximum temperatures reached. Testing if the temperature in the planetesimal ultimately reaches equilibrium with the dust temperature is verified in section B.3. The addition of ammonia into the ice has a significant impact on the ice melting temperature. The effects of these proposed additions on the thermal modelling are shown in section 3.1 and section 3.4 and their implementations are discussed below.

Surface radiation

In the model proposed by Wakita & Sekiya (2011), the surface temperature (where $r = R$) T_R is kept equal to the disk temperature T_0. We introduce black-body radiative cooling to the surface layer. The CPD introduced in section 2.1 is assumed to be optically thick, meaning that the gas surrounding the planetesimal would be heated by the thermal radiation of the planetesimal. However, the orbital velocity of the gas differs by 1% of the Keplerian velocity of the planetesimals (Batygin & Morbidelli 2020), meaning that the heated gas surrounding the planetesimal is continuously replaced with cooler gas. Therefore we assume the temperature of the circumplanetary disk gas surrounding the planetesimal stays constant at T_0. The energy budget for the surface layer is given in Equation 19.

$$Q_R = Q_{^{26}Al} + Q_{\mathrm{cond}} - Q_{\mathrm{rad}} \tag{19}$$

The energy balance computes the total energy in the surface layer Q_R which is a summation of the heating by short-lived radionuclides $Q_{^{26}Al}$ inside the surface layer, heating via conduction by the sub-surface layer Q_{cond} and the heat radiated away Q_{rad}. The aforementioned contributors to the energy budget in the surface layer $Q_{^{26}Al}$, Q_{cond} and Q_{rad} are computed using Equation 20, 21 and 22 respectively.

$$Q_{^{26}Al} = \frac{4}{3}\pi(R_p^3 - (R_p - \Delta r)^3)A_0 e^{(-\lambda_{^{26}Al} t^n)} \tag{20}$$

$$Q_{cond} = 4\pi\bar{K}\left(T_{R-\Delta r}^n - T_R^n\right)R_p(j-1) \tag{21}$$

$$Q_{rad} = 4\pi R_p^2\sigma\left((T_R^n)^4 - T_0^4\right) \tag{22}$$

In the present model, we consider the Stephan-Boltzmann constant σ and the temperature of the sub-surface layer $T_{R-\Delta r}^n$ in K, situated directly beneath the surface layer. The assumption is made that the emissivity of the planetesimal is 1. Relating the energy budget to the temperature increase is done with Equation 23, where the mass of the surface layer M_R is computed. The dependency of surface temperature and layer thickness is discussed in section C.4.

$$T_R^{n+1} = T_R^n + \frac{Q_R\Delta t}{\bar{c}M_R} = T_R^n + \frac{Q_R\Delta t}{\bar{c}\bar{\rho}\frac{4}{3}\pi\left(R_p^3 - (R_p - \Delta R)^3\right)} \tag{23}$$

Refreezing

The liquid water mantle is at constant temperature T_{melt} we assume all liquid water layers are in thermal equilibrium due to the convection of heat from the rocky core through the liquid water mantle to the undifferentiated surface layers. With this assumption, constant heating would be supplied to the cooling outer layers of the planetesimal. To account for this, the top layer of the liquid water mantle is allowed to refreeze according to the inverse equation of Equation 14.

Table 6. Ammonia ice melting temperature coefficients for Equation 24 from Leliwa-Kopystyński et al. (2002).

Sym	Value	Unit
b	7.95×10^{-8}	K Pa^{-1}
a	9.6×10^{-17}	K Pa^{-2}
A	53.8	K
B	650	K
C	4×10^{-8}	K Pa^{-1}

Table 7. Variables used in the numerical model, including base values that are used to analyse the initial parameter variations unless stated otherwise.

Sym	Parameter	Value	Unit
R_p	Planetesimal radius	50	km
f_i	Initial ice fraction	0.632	-
T_0	Initial and background temperature	130	K
Δt	Integration time step	100	yr
Δr	Integration layer thickness	0.025	R_p
t_{start}	time after CAI formation	1.0	Myr
t_{end}	Final time of computation	10.0	Myr
X_{NH_3}	Ammonia mass fraction	0.0	-

Ammonia ice

There is a significant amount of ammonia ice in the CPD icy dust grains with a maximum mass fraction in the ice of 30.7%. Barr & Canup (2008) showed that the duration of accretion to avoid melting due to radiogenic and accretional heating of Callisto increased by 0.1 Myr to τ_{acc}> 0.7 Myr when including only 5% ammonia ice. Ammonia ice decreases the melting temperature of the ice inside the planetesimal $T_{\text{melt}}(X_{NH_3}, P)$, and is proportional to the mass percentage of ammonia ice X_{NH_3} and the pressure P inside the planetesimal in Pa. The melting temperature can be computed using Equation 24 with coefficients provided in Table 6, taken from Leliwa-Kopystyński et al. (2002). This implementation causes the ice in ammonia-rich planetesimals to start melting at lower temperatures.

$$T_{\text{melt}}(X_{NH_3}, P) = 273.15 - bP - aP^2 - AX_{NH_3} - BX_{NH_3}^2 - CPX_{NH_3} \quad (24)$$

To compute the pressure P needed to compute $T_{\text{melt}}(X_{NH_3}, P)$ inside each layer of the planetesimal, Equation 25 is used introducing the gravitational constant G. This assumes the pressure inside the planetesimal is from hydrostatic equilibrium. For $j = 0$, the surface layer is indicated meaning that pressures are computed at the lower boundary of all layers, making sure the temperature at the surface layer is non-zero. The density used in this equation $\bar{\rho}$ is the density of all layers above the current layer j.

$$P = \frac{2}{3} G\pi R_p^2 \bar{\rho}^2 (1 - \frac{j\Delta R}{R_p}) \quad (25)$$

2.3.3. Thermal model parameters

To determine the influence of single parameters on the planetesimal thermal evolution, other constants are kept at fixed values to compare the results. A set of parameters is given in Table 7 that is used as standard values unless stated otherwise. This will show the impact of varying individual initial conditions. For the individual parameter analysis, the initial temperature, ice mass fraction and formation time are based on Wakita & Sekiya (2011)

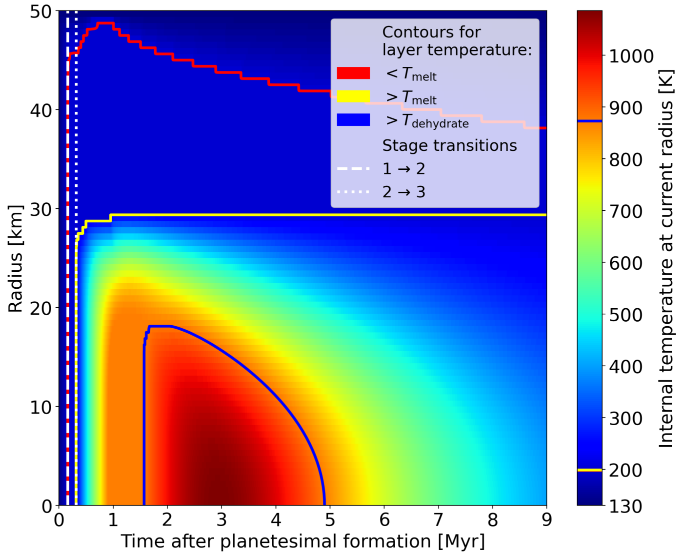

Fig. 4. The interior temperature evolution of a single R_p = 50 km planetesimal, where radius 0 km indicates the core and radius 50 km the surface layer. Contour-lines highlight the boundary conditions of ice melting (red), temperatures exceeding the melting temperature (yellow) and temperatures hot enough for dehydration of hydrated rocks (blue). The stages 1-3 describing initial conditions, ice melting and differentiation and their transitions 1 → 2 and 2 → 3 as defined in Figure 3 are shown in the white dashed/dotted lines.

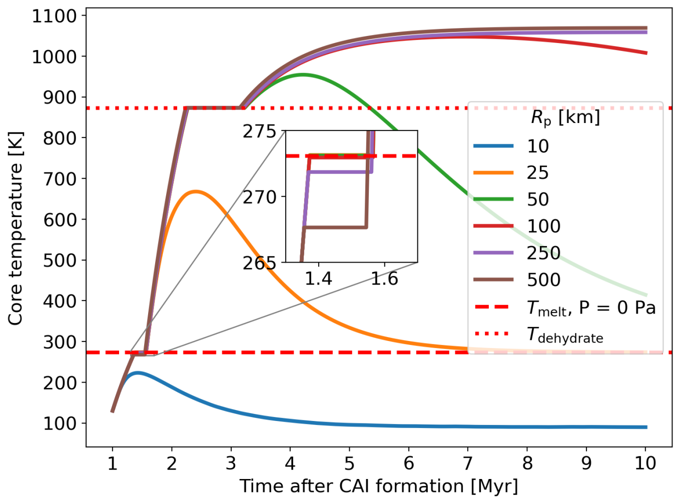

Fig. 5. Core temperature for planetesimals with radius [10, 25, 50, 100, 250, 500] km, with highlighted melting temperature without the effects of pressure and the dehydration temperature. The zoomed-in region shows different melting temperatures for different planetesimal sizes based on internal pressure.

to compare results. Note that the integration layer thickness is based on the total planetesimal radius R_p so that the amount of layers for planetesimals of arbitrary size remains identical. The end of formation t_{end} is in line with typical lifetimes of a CPD of 10 Myr (Podosek & Cassen 1994; Ward & Canup 2010).

3. Results

We trace the interior thermal evolution of a population of CPD planetesimals to derive the resulting interior compositions. For

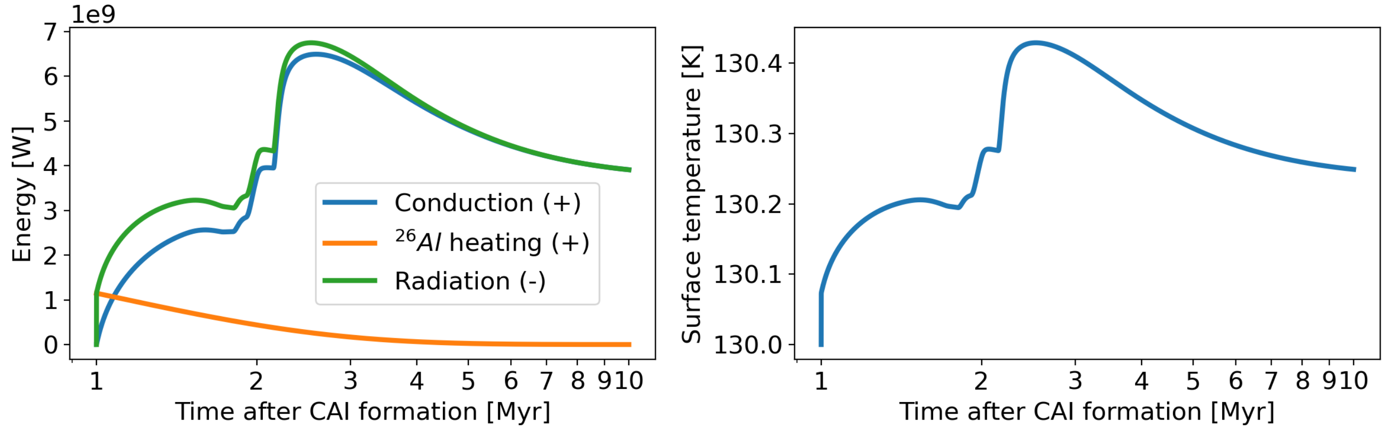

Fig. 6. Surface layer energies and temperature for a planetesimal with radiative surface cooling. (Left) Energies of the three contributing heating/cooling sources (Conduction, ^{26}Al heating and surface radiation) with positive and negative describing heating and cooling. (Right) Surface temperature evolution which is no longer constant and equal to T_0.

an individual planetesimal, we test variations of R_p, T_0, f_i, and $t_{\rm start}$ along with the proposed additions to the thermal model of surface radiation, liquid water refreezing and ammonia ice to assess their role in the planetesimal thermal evolution. These results correspond to a $t_{\rm start}$ = 1 Myr after CAI formation to better visualise the effects of ^{26}Al since radiogenic heating is larger (decreasing by a factor of 2.62 after every 1 Myr) and to standardize our results for comparison to Wakita & Sekiya (2011). Note that this is significantly earlier than what is described in section 1 for the formation of Jupiter itself. Formation times are tested for a sample population formed by the streaming instability to determine different planetesimal compositions, to determine how the composition and internal structure of planetesimals evolve after their formation in the CPD due to the effects of radiogenic heating of ^{26}Al. Additionally, the ammonia concentration in the ice of the CPD is scaled to assess the impact of ammonia on the resulting composition and the delay in producing hydrated silicates.

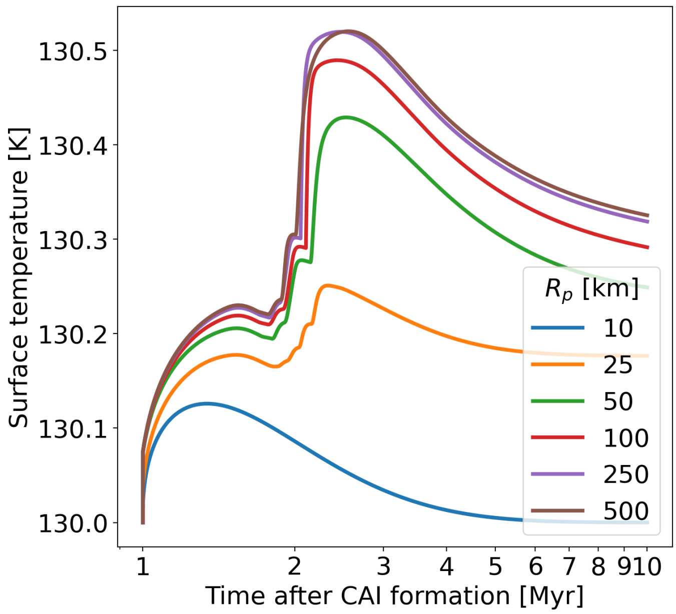

Fig. 7. Surface temperature for varying planetesimal radius [10, 25, 50, 100, 250, 500] km.

3.1. Planetesimal thermal evolution

The interior thermal evolution of the planetesimal with characteristics described in Table 7 is shown in Figure 4. The evolution of the planetesimal follows the different stages described in Figure 3. At its initial state, the planetesimal is a homogeneous undifferentiated ice-rock mixture (stage 1). Heating by ^{26}Al increases the interior temperature until it reaches $T_{\rm melt}$ (stage 2). After the ice has melted, a rocky core and liquid mantle are formed (stage 3). The planetesimal is initiated with a temperature equal to T_0 equal to the surrounding circumplanetary dust temperature. It takes 0.37 Myr for the core to reach $T_{\rm melt}$, after which core-formation separates the rocky core from the liquid mantle. The liquid water mantle is at a temperature $T_{\rm melt}$ and is located at a radius > 30 km. This causes further melting and differentiation of the surface layers as seen by the gradual increasing yellow contour line after 0.57 Myr bordering the rocky core and the red contour line bordering the liquid water mantle. The surface thickness is 1.25 km and is situated between the red contour line and 50 km. line and is The liquid mantle refreezes after 1 Myr which makes the pure ice shell thicken with time and occurs after the formation of the liquid mantle as seen by the red contour line in Figure 4 where the temperature drops below $T_{\rm melt}$.

The maximum temperatures are reached in the core of the planetesimal, after which the core cools due to surface radiation and convection through the liquid mantle.

Increasing planetesimal radius R_p leads to larger maximum temperatures reached in the core as seen in Figure 5. The core temperature is always the hottest layer and gives an indication if ice melting has occurred in the planetesimal since it is the first layer to reach this condition. This is important to determine when compositional changes start. The evolution of the planetesimal's interior composition is discussed in section 3.2. The melting temperature is lower for larger planetesimals due to the higher internal pressure. The core pressure of R_p = 500 km is 643 bar, lowering the melting temperature from the non-pressurised 273.15 K to 267.6 K (without ammonia) according to Equation 24. This is highlighted in Figure 5 in the zoomed-in section where ice melting occurs. For a smaller planetesimal with R_p = 100 km, this effect is reduced and the melting temperature only decreases by a maximum of 0.2 K. Planetesimals with size R_p = 250 and 500 km show similar behaviour by increasing their temperature to 1059 and 1069 K respectively. The planetesimals with R_p = 10, 25 and 50 km reach their maximum temperature of 223, 667 and 954 K respectively in different regimes: no ice melting, ice melting and core/mantle separation and dehydrated rock. Other parameter variations on $t_{\rm start}$, T_0 and f_i have been included in section B.2. Summarising the observations of all the varied parameters:

- Increased **planetesimal radius** leads to larger maximum temperatures reached in the core but no significant delay in reaching aqueous alteration.
- Increased **ice mass fraction** shows that the maximum temperature decreases with increasing ice fraction since only rocky compounds contain SLRN that cause heating. Delay in reaching the aqueous alteration is seen for ice mass fractions > 50%.
- Increased **dust temperature** causes higher maximum temperatures, significantly delaying the ice melting of planetesimals.
- A later **formation time** results in less radiogenic heating because a fraction of ^{26}Al has already decayed, causing lower maximum temperatures reached in the planetesimal.

The effect of refreezing does not change the core temperature of the planetesimal for timescales below $t_{\rm end}$. Testing the refreezing method is done in section B.3. Without refreezing, the core would be insulated by the liquid water mantle at a constant $T_{\rm melt}$ but can now cool by the colder refreezing liquid water mantle.

Replacing the assumption of constant surface temperature equal to T_0 to a new temperature computed from the energy balance from Equation 19 results in a temperature profile shown in the right panel of Figure 6. Conduction and ^{26}Al heating increase temperatures and surface radiation decreases the temperature in the surface layer. The temperature increases by 0.22 K over the first 1 Myr when convection through the liquid water mantle becomes dominant given more layers have differentiated. This results in a maximum surface temperature increase of 0.43 K at 1.5 Myr after planetesimal formation. The magnitude of the surface temperature depends on the CPD temperature, given that surface radiation becomes more powerful for higher T_0 (Equation 22). The sublimation temperature of ice is pressure-dependent. This pressure according to Equation 25 is reached at depths proportional to $\Delta R \sim R - \sqrt{R^2 - P_{\rm sub}}$, indicating sublimation occurs at deeper depths for smaller planetesimals. Larger planetesimals have larger maximum surface temperatures as shown in Figure 7, increasing by 0.5 K for a planetesimal with R_p = 500 km. This can be explained by the ratio of surface energy being radiated proportional to R_p^2, and the energy coming from radiogenic heating being related to the mass of each layer, proportional to R_p^3. For the ice-rich regions in the CPD, the maximum dust- and thus initial surface temperature is 174K. Using the sublimation equation of Brunini & López (2018), the corresponding sublimation pressure $P_{\rm sub}$ is 0.002 Pa. For $R_{p,min}$ = 10 km this results in ΔR = 4×10^{-4} m which is negligible for the ΔR = $0.025R_p$ = 250 m, assuming the only pressure inside the planetesimals comes from the layers above. This study shows a very efficient cooling of the surface and thus no sublimation of ice. The efficiency could be lowered by introducing a lower emissivity representative for planetesimal surfaces alongside heating of gas surrounding the planetesimal. The efficiency would increase with better estimates for the surface area which is currently assumed to be a perfect sphere by including ridges and striations. Decreasing the efficiency of cooling would increase surface temperatures and allow for significant sublimation of ices in the planetesimal.

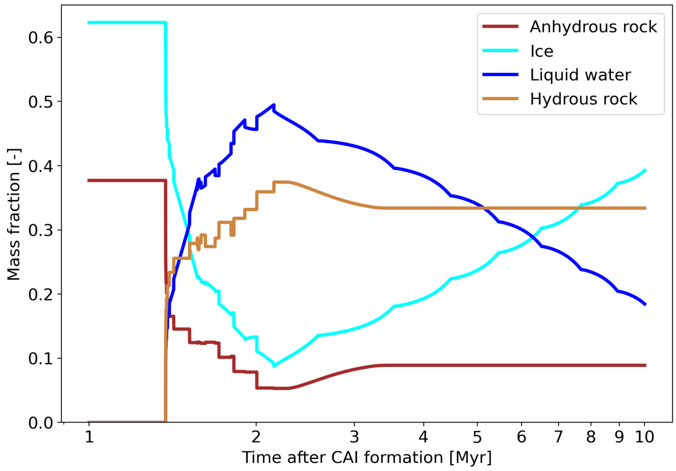

Fig. 8. Compositional evolution of the planetesimal described in Table 7 with different compounds anhydrous rock, ice, liquid water and hydrous rock. The aqueous alteration occurs from 1.37 Myr till 2 Myr after CAI formation seen by the step-wise increase in hydrous rocks for every layer. After 2.15 Myr, the hydrous rocks are dehydrated and converted into anhydrous rock.

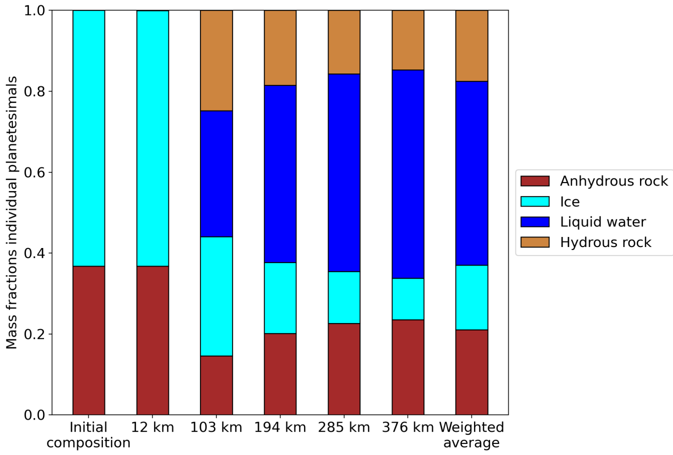

Fig. 9. Resulting composition after thermal evolution using initial conditions from Table 7 of 5 planetesimals with R_p = [12, 103, 194, 285, 376] km along with the initial dust composition on the left and the resulting total composition of the population computed from abundances in Table 3.

3.2. Planetesimal composition evolution

For the base parameters shown in Table 7, the alteration of the planetesimal interior composition is given in Figure 8. Aqueous alteration occurs 0.37 Myr after formation seen by the initial increase of hydrous rocks followed by every next layer that melts causing an increase in the hydrous rock composition. The aliasing between the (hydrous) rocky core and liquid water mantle described in section 2.3 and section C.3 can be seen between 1.5 and 1.7 Myr after CAI formation, where the true radius of the rocky core $R_{r,real}$ computed from the mass fraction differs from the numerical layer boundary $R_{r,num}$. This causes variations

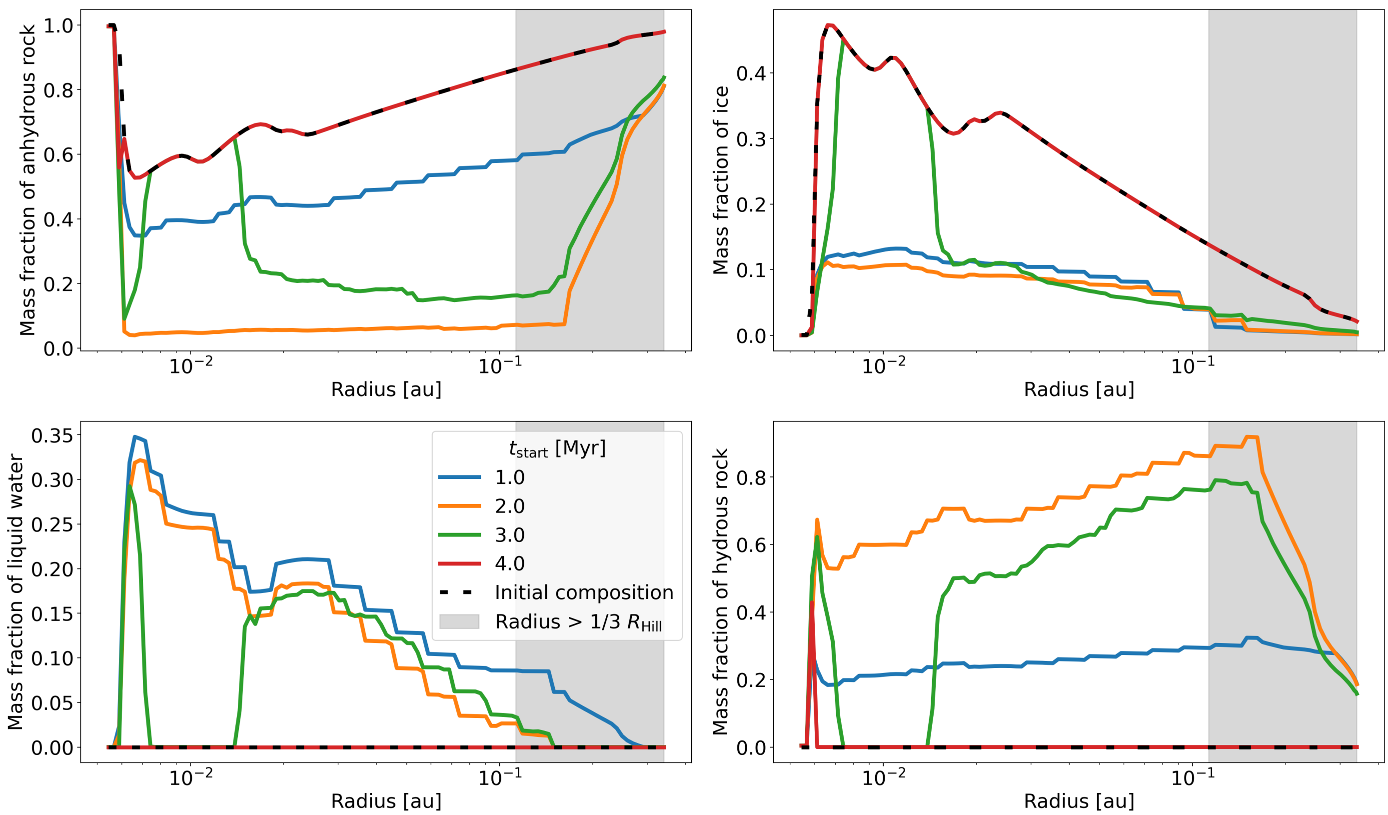

Fig. 10. Weighted averaged planetesimal population composition for thermal evolution using the initial conditions dust temperature, ice mass fraction and ammonia concentration inside the CPD. The start of planetesimal formation is varied for [1, 2, 3, 4] Myr, and the different compounds are (top left) anhydrous rock, (top right) ice (bottom left), liquid water and (bottom right) hydrous rock. The initial conditions for the planetesimals (black dashed line) and the unstable part of the CPD outside 1/3 $R_{\rm Hill}$ (grey area) are shown.

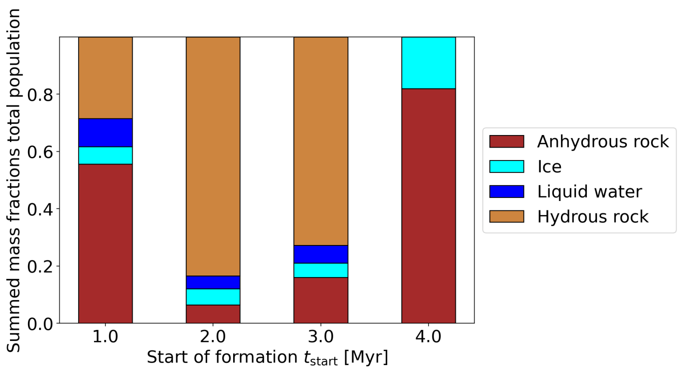

Fig. 11. Total disk-integrated planetesimal composition for formation times ranging from [1,2,3,4] Myr after CAI formation. The unstable region outside 1/3 $R_{\rm Hill}$ is excluded from the disk-integrated composition .

in the mass fractions of hydrous rock and liquid water. After 2 Myr, liquid water freezes. The core layers reach the dehydration temperature, meaning that anhydrous rocks and liquid water is created from the dehydration of hydrous rock. The composition of this planetesimal has converged to 9% anhydrous rock and 33% hydrous rock after 10 Myr respectively, with liquid water still freezing.

3.3. Planetesimal population composition evolution inside the CPD

Figure 5 shows that larger planetesimals are subjected to more temperature increases due to radiogenic heating and an increased core pressure which lowers the melting temperature. Given their larger internal temperatures, larger planetesimals are thus more likely to undergo aqueous alteration and differentiation. This can be seen in Figure 9, where the resulting composition of the planetesimal population of Table 3 with CPD conditions (ice mass fraction, dust temperature and ammonia fraction) being equal to Table 7 is given. Aqueous alteration does not occur for R_p = 12 km and the composition remains unaltered/primordial. The effects of dehydration increase for larger planetesimals since their mass fraction of hydrous rock is smaller. Since the mass of the population is shifted to larger planetesimals shown in Figure 2, the resulting total composition of the population follows the composition of massive planetesimals. The total composition of the population is [0.23, 0.16, 0.45, 0.16] for anhydrous rock, ice, liquid water and hydrous rock respectively.

Repeating the previously performed analysis for the CPD conditions from section 2.1 for starting times of [1, 2, 3, 4] Myr after CAI formation yields the profiles for the four compositions given in Figure 10. For t_{start} = 4 Myr, radiogenic heating only negligibly increases the interior temperature of the planetesimal and no hydrous material is produced, similarly for t_{start} = 3 Myr between 7.14×10^{-3} and 1.44×10^{-2} au. Summing all mass fractions obtained in Figure 10 for all different formation times results in the total CPD composition shown in Figure 11, where

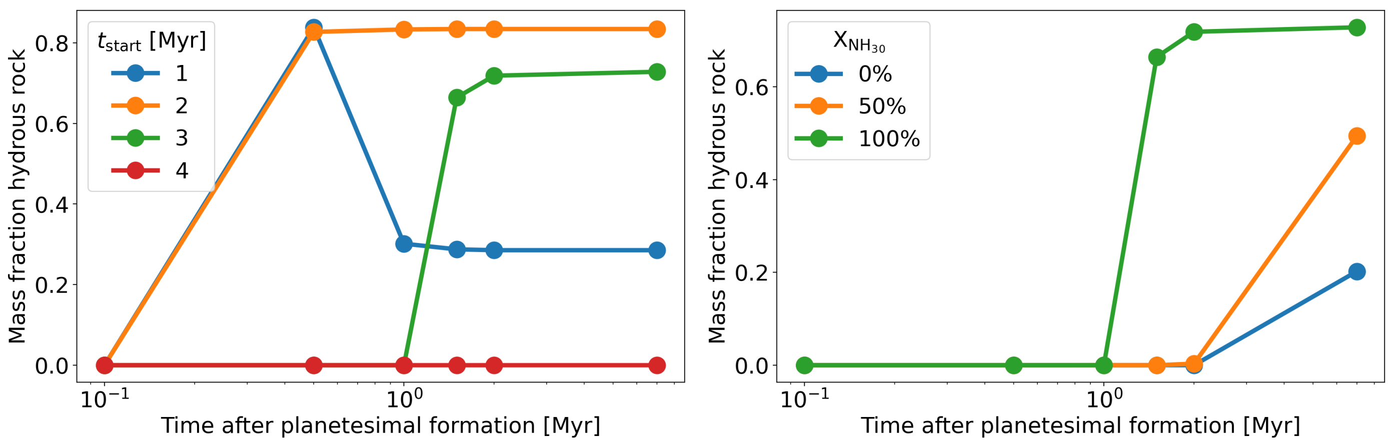

Fig. 12. Total disk-integrated planetesimal mass fraction of hydrous rock after $[0.1, 0.5, 1.0, 1.5, 2.0, t_{end}]$ Myr of thermal evolution for (Left) formation times t_{start} of [1, 2, 3, 4] Myr after CAI formation and (Right) scaled ammonia concentrations of [0, 50, 100] of $X_{NH_{30}}$.

the unstable region outside 1/3 R_{Hill} is excluded from the disk-integrated composition . The maximum amount of hydrous rocks occurs at t_{start} 2 Myr with a value of 83%. For hydrous rocks to be created, temperatures need to reach above T_{melt} but stay below $T_{dehydrate}$ to prevent dehydration, explaining the lower mass fractions of hydrous rock t_{start} = 1 Myr (too much dehydration) and t_{start} = 3 Myr (less planetesimals reach aqueous alteration). Their hydrous rock mass fractions are 29% and 73% respectively. The weighted average mass fractions of hydrous rock of the planetesimals at $[0.1, 0.5, 1.0, 1.5, 2.0, t_{end}]$ Myr after t_{start} is shown in Figure 12. This shows that aqueous alteration starts after 0.5 Myr for t_{start} = 1 and 2 Myr and after 1.5 Myr for t_{start} = 3 Myr. Dehydration is observed after 1 Myr for t_{start} = 1 Myr.

The initial ice fraction plays an important role in the generation of hydrous rocks. From Figure B.3 it is clear that a lower ice mass fraction causes higher temperatures due to the presence of SLRN in the rocks. Besides the extra heat being generated when ice is lacking, initial ice is also required to produce the hydrous rocky compounds. The location in the disk where the maximum amount of hydrous rocks are being generated in the population is similar for all starting times (excluding t_{start} 4.0 Myr) and is located at a radius of 0.150 au, with conditions in the CPD: T_0 = 51.2 K, f_i = 0.11 and X_{NH_3} = 0.196. This location is outside the stable region of the CPD inside $1/3R_{Hill}$. Inside the stable region near the ice-line, hydrous rocks show a local maximum for all formation times due to the relatively high circumplanetary dust temperatures of 170-200 K causing melting even for late formation or high ice mass fractions.

3.4. Ammonia concentration

The core temperatures of planetesimals with characteristics given in Table 7 for varying ammonia concentrations up to 30% are shown in Figure 14. A concentration of X_{NH_3} = 30% the lowers the melting temperature from the original 273.15 K to 198.5 K. Given the lower melting temperature, planetesimals with a higher concentration finish their aqueous alteration sooner since a smaller fraction of SLRN has decayed and ultimately reach higher core temperatures. The time of complete melting is reached 0.25 Myr earlier for 30% ammonia compared to 0%.

The impact of the ammonia concentration in the ice of planetesimals can be seen in Figure 13 by performing the same analysis as in section 3.3 for t_{start} = 3 Myr and varying the original ammonia concentration in the CPD $X_{NH_{30}}$ by 100%, 50% and 0%. This formation time is chosen since it is between high concentrations of hydrous rock at 2 Myr and no hydration at 4 Myr. The region inside the CPD where planetesimals do not show deviations from the initial conditions is 6.55 and 10.6 times wider for 50% and 0% $X_{NH_{30}}$. Taking the weighted average from Figure 13 of all locations in the CPD excluding the unstable region outside 1/3 R_{Hill} results in the total composition for the three cases shown in Figure 15. This shows that the mass fraction of hydrous rock is 73%, 49% and 20% for ammonia concentration with values of 100%, 50% and 0% of $X_{NH_{30}}$. By lowering the melting temperature of ice, an increased ammonia concentration can compensate for the lower radiogenic heating, creating the same amount of rocks compared to an ammonia-free condition with an earlier formation time. Similar to Figure 10, hydrous rocks are formed near the ice-line with no significant effect of decreased ammonia concentration. The weighted average mass fractions of hydrous rock of the planetesimals at $[0.1, 0.5, 1.0, 1.5, 2.0, t_{end}]$ Myr for varying $X_{NH_{30}}$ is shown in Figure 12. For t_{start} = 3 Myr and 50% and 0% $X_{NH_{30}}$, aqueous alteration of planetesimals only occurs after 2.0 Myr. With the introduction of 100% $X_{NH_{30}}$, this timescale is reduced to 1.5 Myr. This means ammonia can potentially hydrate planetesimals that were originally lost due to inward migration.

It has to be noted that the only property of ammonia ice taken into account is its ability to lower the melting temperature for increasing concentration. Parameters such the thermal properties, density and resulting chemical reactions as given in Table 5, Equation 10 and Equation 17 are all focused on water ice. The most notable difference is the thermal conductivity K_{NH_3} = 1.2 W m^{-1} K^{-1}, which is approximately half of K_i = 2.2 W m^{-1} K^{-1} (Kargel 1992; Lorenz & Shandera 2001; Desch et al. 2009). The thermal diffusivity decreases for a lower thermal conductivity shown in Equation 9, meaning that the temperature increase due to conduction in a layer decreases by the second term in Equation 3. This thus counteracts the ability of ammonia to produce more hydrous materials by lowering the increase in temperature inside a planetesimal. At most, the total mass fraction of ammonia in a planetesimal in the CPD is 10% at 0.024 au (f_i = 34% and X_{NH_3} = 30.4%), decreasing $\bar{K}$ by 1.8%.

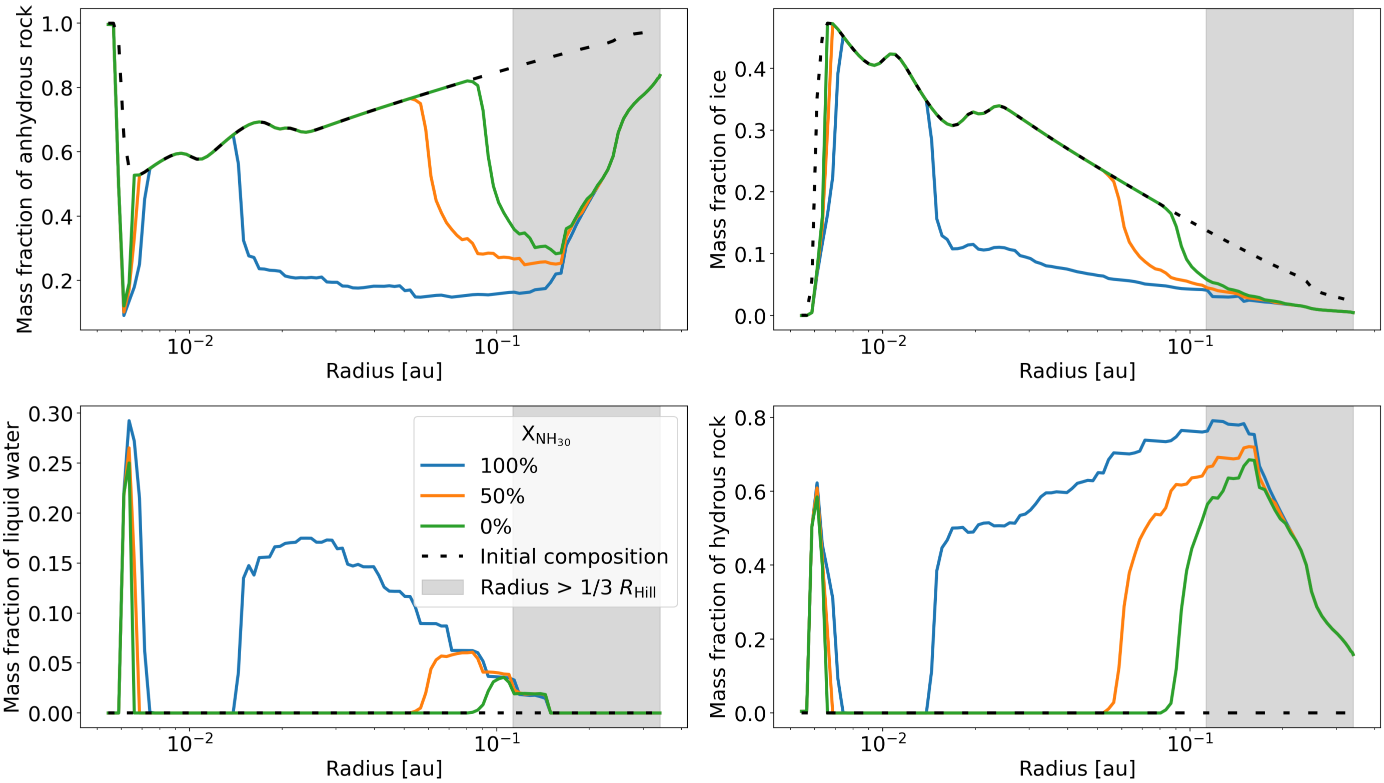

Fig. 13. Resulting planetesimal population composition for every initial condition in the CPD. Start of formation is fixed at t_{start} = 3.0 Myr and three different cases are analysed where the original ammonia concentration $X_{NH_{30}}$ is scaled [100%, 50%, 0%]. where the 100% condition is similar to Figure 10. The different compounds are (top left) anhydrous rock, (top right) ice (bottom left), liquid water and (bottom right) hydrous rock.

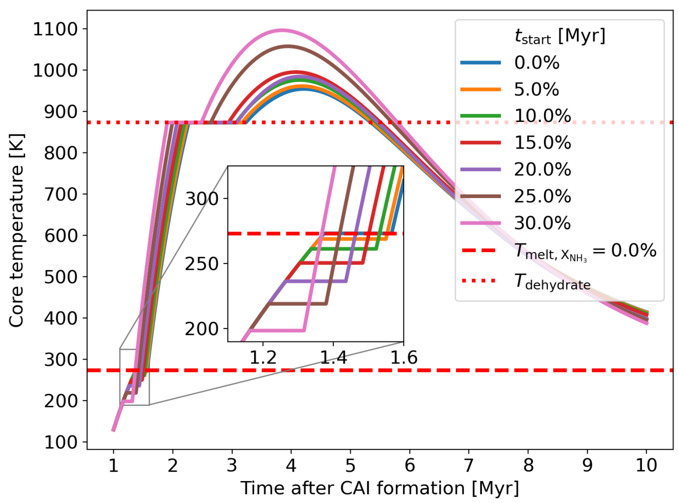

Fig. 14. Core temperature for planetesimals with initial concentration of ammonia ice of [0,5,10,15,20,25,30] % after CAI formation, with highlighted melting- and dehydration temperature for ammonia-free ice. The region between 1.1 and 1.6 Myr is shown in a zoomed-in graph to highlight the different melting temperatures and time of complete melting.

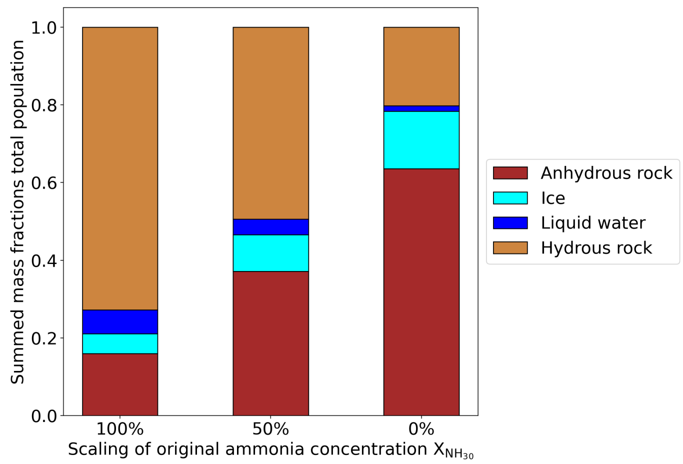

Fig. 15. Summed population composition for all locations in the CPD for different scaling of the original CPD ammonia concentration $X_{NH_{30}}$ of [100%, 50%, 0%] with t_{start} = 3 Myr after CAI formation. The unstable region outside 1/3 R_{Hill} is excluded from the disk-integrated composition .

4. Discussion

Icy planetesimals are formed by the streaming instability taking initial conditions for temperature, ice mass fraction and ammonia concentration in the ice from the CPD. Radiogenic heat from ^{26}Al causes temperature variations that drive compositional alterations. Aqueous alteration hydrates the originally anhydrous rock, which then differentiates to form a rocky core and liquid water mantle. If temperatures increase further, the hydrated rock dehydrates back into anhydrous rock and liquid water. The planetesimals formed by the streaming instability are assumed to serve as the building blocks of the Galilean moons by colliding together to form larger objects. The formation of Jupiter is

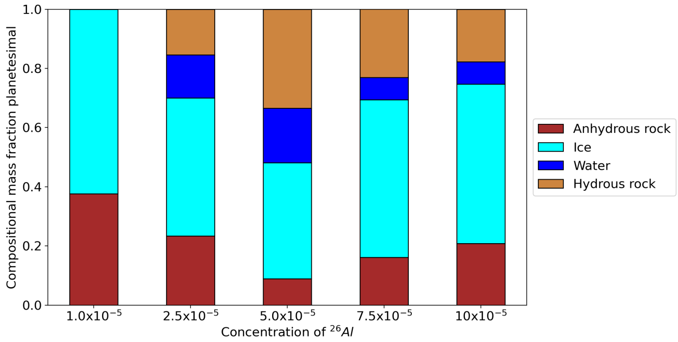

Fig. 16. Composition of a planetesimal with characteristics shown in Table 7 with different concentrations of ^{26}Al [1.0, 2.5, 5.0 , 7.5, 10.0] $\times 10^{-5}$.

expected to have reached a runaway gas accretion phase between 3.46 and 3.94 Myr after CAI formation. The CPD in which we expect the moons to be forming most likely forms at the end of Jupiter's runaway gas accretion. We assume over time the water and ice of the icy planetesimals are completely lost. This means hydrated silicates remain inside the forming moons, able to release their water compound after heating to the surface.

Assuming all liquid water/ice is removed from the colliding planetesimals, Io should form from a planetesimal population with no hydrous silicates. For t_{start} = 3 Myr, the hydration of silicates only occurs 1.5 Myr after formation. The formation of Io could thus be explained by planetesimals that combined on timescales up until 1 Myr to prevent aqueous alteration inside the planetesimals. If Io formed with included hydrated silicates, dehydration of these hydrated rocks would not be possible with only SLRN heating since even for formation times much before the expected formation such as t_{start} = 1 Myr shows 24% hydrated rocks after dehydration.

For t_{start} = 4 Myr, the remaining ^{26}Al fraction is 18 times smaller compared to t_{start} = 1 Myr and no compositional alterations occur. This limits the formation of Europa since the planetesimals that formed Europa should have formed before 4 Myr after CAI formation if we assume hydrated silicates are the source of Europa's ice content. Besides the planetesimals forming before t_{start} = 4 Myr, they should have evolved for at least 1.5 Myr in the CPD in order for ^{26}Al to hydrate silicates. The observed hydrous rock mass fraction for t_{start} = 3 Myr after 1.5 Myr is 66%, able to release a water/ice mass fraction of 6.3%. This is in line with the estimates between 5-8% of the currently observed ice content on Europa (Schubert et al. 2004). The type-I migration timescale of bodies with $R_p \sim 400$ km are $\tau_I > 10^6$ Myr for $\Sigma_g \sim 400$ g cm^{-1}, the largest gas surface densities observed in this CPD (Tanaka et al. 2002; Canup & Ward 2009).

The interior of Ganymede is expected to be fully differentiated, and the interior of Callisto is only partially differentiated (Schubert et al. 2004). We have shown that differentiation exclusively by ^{26}Al heating is not possible for planetesimals that have formed after t_{start} = 4 Myr. For Callisto to remain only partly differentiated, it should have formed after t_{start} = 4 Myr. Estimates using both accretional and radiogenic heating show a similar result where Callisto must not finish its formation earlier than 4 Myr after CAI formation to prevent differentiation (Barr & Canup 2008).

The numerical errors as described in Appendix C include two significant errors: representing the population as 5 planetesimals and the planetesimal layer thickness. Their introduced errors on the hydrous rock mass fraction ϵ_h are approximately ∼1% and ∼8% respectively. For the mass fraction of hydrous rocks of 66% formed 1.5 Myr after t_{start} = 3 Myr after CAI formation, the relative error is 66±6%. This means the ice mass fraction is able to be dehydrated from a hydrated core is 6.3±0.6%. This value is still well inside the range expected for the low ice mass fraction of Europa of ∼5-8%.

The concentration of ^{26}Al is relatively well known for our solar system but might differ for other systems (Gounelle 2015). Varying the estimate used for the solar system of 5.0×10^{-5} is done in Figure 16 already shows the potential of ^{26}Al to drastically change the resulting composition of a 50 km planetesimal, let alone the entire population of planetesimals. Here, the original concentration of ^{26}Al shows the highest amount of hydrated rocks, with lower concentrations not (fully) reaching aqueous alteration and higher concentrations being subjected to more dehydration in the rocky core.

5. Conclusion

We have performed numerical simulations on the thermal evolution of planetesimal populations by ^{26}Al heating and from analysing the resulting compositions we can conclude:

1. Planetesimals forming after t_{start} = 4 Myr show no melting of ices, hydration of rocks and differentiation of the ice/rock mixtures. If Europa's water originated from planetesimal silicates hydrated in the CPD, they could have formed no later than 4 Myr and survived in the CPD for at least 1.5 Myr.
2. Io should have formed and lost its ice on timescales shorter than 1.5 Myr to prevent hydration of silicates. If Io did form from planetesimals with hydrated silicates, dehydration of these hydrated rocks would not be possible for SLRN heating.
3. For Callisto to remain only partially differentiated, planetesimals should have formed no earlier than 4 Myr. If the differentiation of Ganymede started before its finishing accretion, planetesimals should have formed before 4 Myr.
4. As the total planetesimal mass is dominated by the largest objects, the bulk composition in the CPD is dependent on their interior evolution, which is weighted towards more hydrated silicates.
5. The influence of ammonia to lower the melting temperature of ice/rock mixtures allows for the hydration of planetesimals at later times after CAI formation. For t_{start} = 3 Myr, ammonia reduces the time to reach aqueous alteration from > 2 Myr to 1.5 Myr.

References

Abod, C. P., Simon, J. B., Li, R., et al. 2019, The Astrophysical Journal, 883, 192
Audi, G. & Wapstra, A. 1995, Nuclear Physics A, 595, 409
Barr, A. C. & Canup, R. M. 2008, Icarus, 198, 163
Batygin, K. & Morbidelli, A. 2020, The Astrophysical Journal, 894, 143
Bierson, C. J. & Nimmo, F. 2020, The Astrophysical Journal letters, 897
Bierson, C. J. & Steinbrügge, G. 2021, The Planetary Science Journal, 2
Brunini, A. & López, M. C. 2018, Monthly Notices of the Royal Astronomical Society, 479, 1392
Canup, R. M. & Ward, W. R. 2002, The Astronomical Journal, 124
Canup, R. M. & Ward, W. R. 2009, in Europa (Tucson, Arizona: University of Arizona Press), 59–83
Castillo-Rogez, J. C. & Lunine, J. I. 2010, Geophysical Research Letters, 37
Chronological Scientific Tables. 2010, edited by National Astronomical Observatory of Japan, Maruzen Co.
Davis, A. M., Alexander, C. M. O., Ciesla, F. J., et al. 2014, Protostars and Planets VI (University of Arizona Press), 809–831

Desch, S. J., Cook, J. C., Doggett, T., & Porter, S. B. 2009, Icarus, 202, 694
Dodson-Robinson, S. E., Willacy, K., Bodenheimer, P., Turner, N. J., & Beichman, C. A. 2009, Icarus, 200, 672
Dwyer, C., Nimmo, F., Ogihara, M., & Ida, S. 2013, Icarus, 225, 390
Garrod, R. T. & Herbst, E. 2006, Astronomy and Astrophysics, 457, 927
Gounelle, M. 2015, Astronomy&Astrophysics, 582
Hay, H. C. F. C., Trinh, A., & Matsuyama, I. 2020, Geophysical Research Letters, 47, e2020GL088317
Huang, W., Audi, G., Wang, M., et al. 2017, Chinese Physics C, 41, 030002
Jacobsen, B., Yin, Q., Moynier, F., et al. 2008, Earth and Planetary Science Letters, 272, 353
Johansen, A., Blum, J., Tanaka, H., et al. 2014, Protostars and Planets VI (University of Arizona Press), 547–570
Kamp, I., Thi, W. F., Woitke, P., et al. 2017, Astronomy and Astrophysics, 607, A41
Kamp, I., Tilling, I., Woitke, P., Thi, W. F., & Hogerheijde, M. 2010, Astronomy and Astrophysics, 510, A18
Kargel, J. S. 1992, Icarus, 100, 556
Kargel, J. S., Kaye, J. Z., Head, J. W., et al. 2000, Icarus, 148, 226
Legates, D. R. 2005, Encyclopedia of World Climatology (Dordrecht: Springer Netherlands), 450–451
Leliwa-Kopystyński, J., Maruyama, M., & Nakajima, T. 2002, Icarus, 159, 518
Lichtenberg, T., Golabek, G. J., Burn, R., et al. 2019, Nature Astronomy, 3, 307
Lodders, K. 2019, The Oxford Research Encyclopedia of Planetary Science
Lorenz, R. D. & Shandera, S. E. 2001, Geophysical Research Letters, 28, 215
Lunine, J. I. & Stevenson, D. J. 1982, Icarus, 52, 14
Martin, R. G. & Lubow, S. H. 2011, Monthly Notices of the Royal Astronomical Society, 413, 1447
McElroy, D., Walsh, C., Markwick, A. J., et al. 2013, Astronomy and Astrophysics, 550, A36
McKinnon, W. 2006, Lunar and Planetary Science XXXVII, 2444
Monteux, J., Golabek, G., Rubie, D., Tobie, G., & Young, E. 2018, Space Science Reviews, 214
Mosqueira, I. & Estrada, P. R. 2003, Icarus, 163, 198
Murphy, D. M. & Koop, T. 2005, Quarterly Journal of the Royal Meteorological Society, 131, 1539–1565
Norris, T. L., Gancarz, A. J., Rokop, D. J., & Thomas, K. W. 1983, Journal of Geophysical Research, 88, B331
Nozaki, W., Nakamura, T., & Noguchi, T. 2006, Meteoritics & Planetary Science, 41, 1095
Oberg, N., Kamp, I., Cazaux, S., & Rab, C. 2020, Astronomy and Astrophysics, 638, A135
Ogihara, M. & Ida, S. 2012, The Astrophysical Journal, 753, 60
Owen, T. & Encrenaz, T. 2003, Space Science Reviews, 106, 121
Podosek, F. A. & Cassen, P. 1994, Meteoritics, 29, 6
Rugel, G., Faestermann, T., Knie, K., et al. 2009, Physycal Review Letters, 103, 072502
Schramm, D. & Wasserburg, G. 1970, The Astrophysical Journal, 162, 57
Schubert, G., Anderson, J. D., Spohn, T., & McKinnon, W. B. 2004, Jupiter. The planet, satellites and magnetosphere., Vol. 1 (Cambridge University Press), 281–306
Shabram, M. & Boley, A. C. 2013, The Astrophysical Journal, 767, 63
Simon, J. B., Armitage, P. J., Li, R., & Youdin, A. N. 2016, The Astrophysical Journal, 822, 55
Tanaka, H., Takeuchi, T., & Ward, W. R. 2002, The Astrophysical Journal, 565, 1257
Thi, W. F., Woitke, P., & Kamp, I. 2011, Monthly Notices of the Royal Astronomical Society, 412, 711
Tobie, G., Lunine, J., Monteux, J., Mousis, O., & Nimmo, F. 2014, Titan: Interior, Surface, Atmosphere, and Space Environment, 29
Tomeoka, K. & Buseck, P. R. 1988, Geochimica et Cosmochimica Acta, 52, 1627
Trappitsch, R., Boehnke, P., Stephan, T., et al. 2018, The Astrophysical Journal Letters, 857
Wakita, S. & Sekiya, M. 2011, Earth, Planets and Space, 63, 1193
Wang, H., Weiss, B. P., Bai, X.-N., et al. 2017, Science, 355, 623
Ward, W. R. & Canup, R. M. 2010, The Astronomical Journal, 140, 1168
Weiss, B. P. & Bottke, W. F. 2021, AGU Advances, 2
Woitke, P., Kamp, I., & Thi, W.-F. 2009, Astronomy and Astrophysics, 501, 383
Yomogida, K. & Matsui, T. 1983, Journal of Geophysical Research: Solid Earth, 88, 9513
Youdin, A. N. & Goodman, J. 2005, Theh Astrophysical Journal, 620, 459

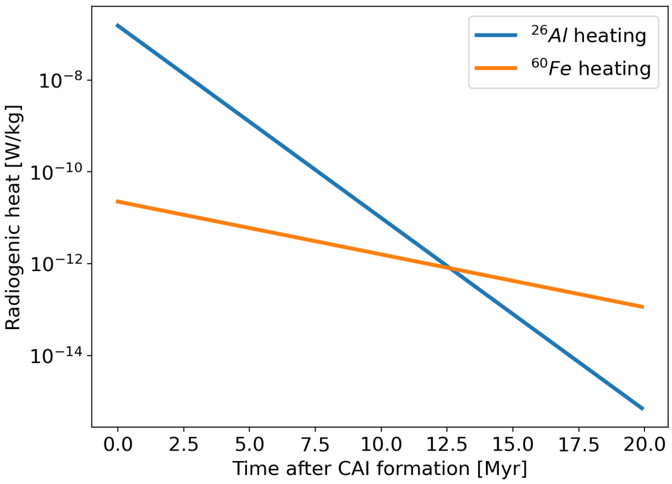

Fig. B.1. Comparison between the heat produced by a kg of rock inside a planetesimal by the decay of SLRN ^{26}Al and ^{60}Fe. The latter becomes dominant after 12.6 Myr after CAI formation.

Appendix A: Circumplanetary Disk Ambient Conditions modelling

Properties of the circumplanetary disk are derived from the 2D radiation-thermochemical disk modelling code ProDiMo [1] (**Pro**toplanetary **Di**sk **Mo**del) (Woitke et al. 2009; Kamp et al. 2010; Thi et al. 2011). The gas and dust temperature in the highly optically-thick midplane are calculated using a radiative transfer diffusion approximation. We adopt the 'large' chemical network described in Kamp et al. (2017) of 235 atomic and molecular species and 13 elements. Reaction rates are adopted from the UMIST2012 database (McElroy et al. 2013). The formation of ices occurs by physisorption of molecules directly from the gas-phase to a dust grain surface. Ices sublimate from grains either thermally or via photo- or cosmic-ray induced desorption. The assumed adsorption energy of ammonia is 5534 K (Garrod & Herbst 2006).

The CPD is assumed to be a 'gas-starved' disk which does not contain simultaneously the refractory mass required to form all four Galilean satellites (Canup & Ward 2002). Hence we consider the case where repeated episodes of planetesimal formation contribute to the slow accumulation of large solids and accretion of satellites. All properties are extracted at the midplane as this is where we expect densities to reach the critical value required to initiate the streaming instability.

Appendix B: Model tests

Appendix B.1: Comparing SLRN ^{26}Al and ^{60}Fe

The heat production of ^{26}Al and ^{60}Fe per kg of rock inside a planetesimal are shown in Figure B.1, where the heat produced is computed using Equation 5. The parameters for ^{26}Al are given in Table 4 and the parameters for ^{60}Fe are given in Table B.1. At the time of CAI formation, heat produced by ^{26}Al is $2.6{\times}10^4$ times larger. After 12.6 Myr, the heat produced by the two SLRN is similar, with ^{60}Fe being more dominant after.

[1] https://www.astro.rug.nl/ prodimo/

Table B.1. Constants of short-lived radionuclide ^{60}Fe.

Sym	Parameter	Value	Unit	Source
f_{Fe}	Fe Abundance	0.186	-	(1)
$f_{^{60}Fe}$	^{60}Fe Abundance	3.8×10^{-8}	-	(2)
$\lambda_{^{60}Fe}$	Decay constant	2.62×10^{-7}	yr^{-1}	(3)
$E_{^{60}Fe}$	Decay energy	0.237	MeV	(4)
$m_{^{60}Fe}$	Nucleus mass	59.9340769	u	(4)

References. (1) Lodders (2019); (2) Trappitsch et al. (2018); (3) (Rugel et al. 2009); (4) Audi & Wapstra (1995)

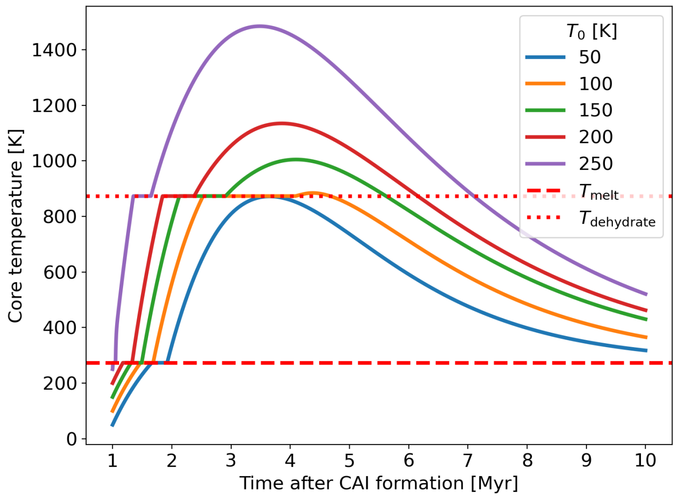

Fig. B.2. Core temperature for planetesimals with initial and dust temperature [50, 100, 150, 200, 250] K, with highlighted melting- and dehydration temperature.

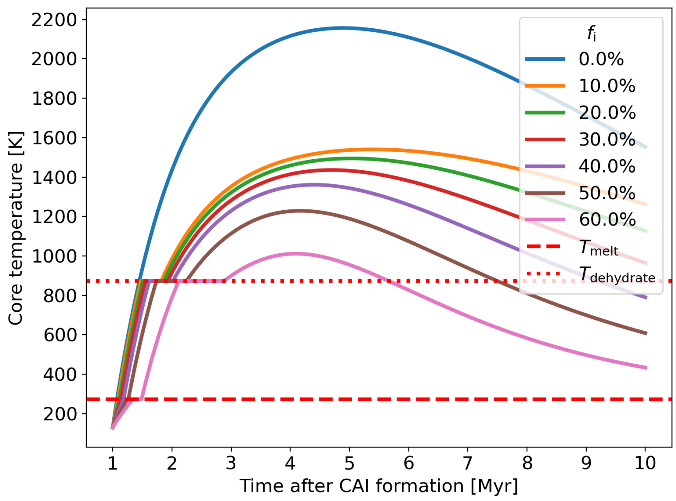

Fig. B.3. Core temperature for planetesimals with initial ice mass fractions [0, 10, 20, 30, 40, 50, 60] %, with highlighted melting- and dehydration temperature.

Appendix B.2: Parameter variations

Parameter variations are performed for T_0, f_i and t_{start}. The default settings from Table 7 are used. For all variations, the constant temperature regions where ice melting and the dehydration reaction occur at T_{melt} and $T_{dehydration}$ respectively are indicated.

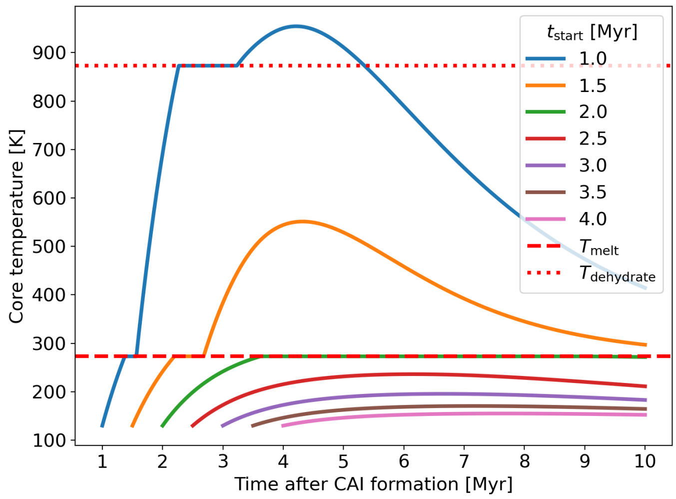

Fig. B.4. Core temperature for planetesimals formed $[1, 1.5, 2.0, 2.5, 3.0, 3.5, 4.0]$ Myr after CAI formation, with highlighted melting- and dehydration temperature.

Increasing **initial planetesimal temperature** T_0 results in higher maximum temperatures in Figure B.2 of 872 K and 1484 for T_0 = 50 K and 250 K respectively. At the start of formation at 1 Myr, the different initial temperatures of the planetesimals can be seen. For the planetesimals formed at higher temperatures, the melting temperature is reached at an earlier time. This time of reaching a core temperature of T_{melt} differs by 0.6 Myr between a planetesimal formed at 250 K or at 50 K. This value is significant with respect to the half-life of ^{26}Al ($t_{1/2,^{26}Al}$ = 0.717 Myr), meaning that the amount of radioactive material has approximately halved between the time ice melting is reached for the two different initial temperatures, causing less radiogenic heating for the lowest T_0. This can be observed in the gradient of the core temperature after ice melting, which is steeper for higher dust temperatures.

Increasing the initial **ice mass fraction** f_i is done in Figure B.3. This shows that the maximum temperature decreases with increasing ice fraction since only rocky compounds contain SLRN that cause heating. The maximum temperatures seem to converge to f_i = 10% making the ice-free an outlier. For this condition, no compositional changes occur and the planetesimal consists of anhydrous rock. Furthermore, there is no creation of a rocky core or a water mantle. The core radius R_r is dictated by f_i since the mass is distributed between rocks and ice.

A later **formation time** t_{start} results in less radiogenic heating because a fraction of ^{26}Al has already decayed, causing lower maximum temperatures reached in the planetesimal. This is shown in Figure B.4, where planetesimals are analysed with different formation times. A formation time of 2 Myr is already too delayed to allow complete ice melting. For formation times later than 2 Myr, T_{melt} is not reached and ice does not melt anywhere in the planetesimal. A difference in core temperature of 734 K is observed between planetesimals formed at 1 or at 3 Myr.

Appendix B.3: Refreezing and long term thermal evolution

As the core evolves with time, its temperature can decrease until it reaches Tm. In this case, liquid water can refreeze. This is shown in Figure B.5 using planetesimal characteristics from Table 7, where the evolution is followed up to 40 Myr. This increase in t_{end} does not correspond to typical lifetimes of CPDs of around 10 Myr and a few Myr for the stellar nebula (Podosek & Cassen 1994; Ward & Canup 2010). In the present case, our goal is to show the long term effects of the addition of refreezing. Only after 21.4 Myr after formation does the core temperature deviate when introducing refreezing. By then, the temperature in the core has converged to the constant temperature of ice, where it remains for the case without refreezing. With refreezing, the liquid water mantle is converted to ice and allows the core to converge to T_0.

The temperature inside the planetesimal should ultimately converge back to T_0 since radiogenic heating decays and the radiative surface cooling stays the same. To verify this, the thermal evolution is extended to 100 Myr (not physically correct for a CPD around Jupiter). In Figure B.6 can be seen that the core temperature (the hottest layer inside the planetesimal) converges to 10^{-3} % of the initial condition T_0.

Appendix B.4: Differentiation

The model assumes differentiation of layers inside the planetesimals after the complete melting of ice inside a layer. This assumption separates the newly formed rocky core from the still unmelted ice and anhydrous rock in the top layers by introducing the liquid water mantle. The radiogenic heat generated in the rocky core is assumed to directly convect through the liquid water mantle to the non-melted surface layers. Figure B.7 shows that the hydrous rock generated by differentiation decreases by 3.5% when excluding differentiation. Even though dehydration occurs in the rocky core of the differentiated planetesimal, the amount of hydrated rocks is still larger. The total temperature reached in the core is lower compared to the case with differentiation, but having the ^{26}Al homogeneously distributed throughout the body without the rocky contents sinking to the core causes all layers to heat at similar rates. This also explains the difference between the liquid water and ice formed, since the surface layers of the differentiated planetesimal cool faster than the non-differentiated planetesimal since the radiogenic material is not homogeneously distributed. The justification to assume instantaneous layer differentiation after melting is due to the short timescales for such processes of 0.22 years (Wakita & Sekiya 2011), being much shorter than the integration time of 100 years used in this work.

Appendix C: Numerical errors

Appendix C.1: Planetesimal histogram sampling

Due to computational limitations, the planetesimal population from Table 3 in section 2.2 is represented as 5 planetesimals. The compositional error percentages compared to populations with increasing resolution of [5, 10, 25, 100] planetesimals using variables from Table 7 is shown in Figure B.4. The error percentages for water ϵ_w and hydrous rock ϵ_h do not exceed 1%, with the error percentages in anhydrous rock ϵ_r an ice ϵ_i around 4-5%. The error percentages are also scaled w.r.t. their total mass fraction in the population.

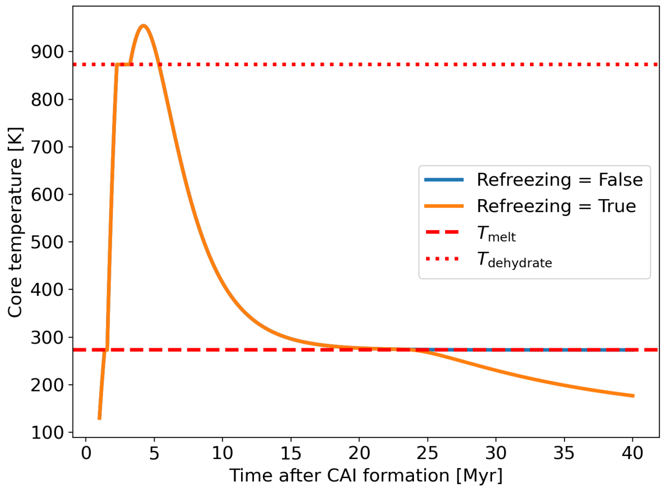

Fig. B.5. Core temperature for planetesimals with and without refreezing of liquid water, with highlighted melting- and dehydration temperature for ammonia-free ice. The end time of computation is extended to 40.0 Myr after CAI formation.

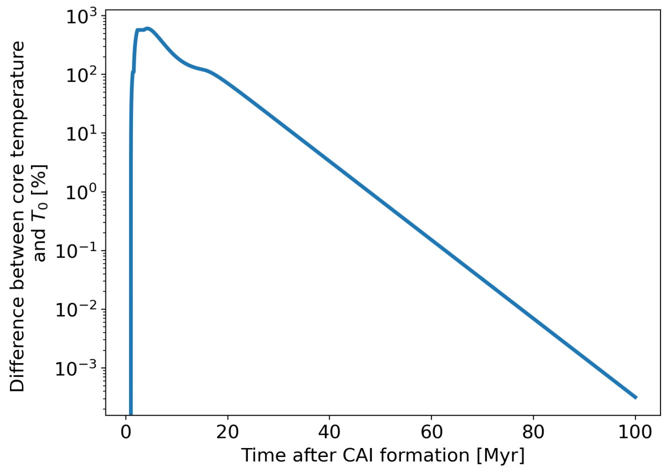

Fig. B.6. Long term thermal evolution of the difference between the core temperature of a planetesimal with characteristics shown in Table 7 and the dust temperature T_0.

Table B.2. Error percentage ϵ of weighted average planetesimal population composition with settings from Table 7, comparing a population sampled with 5 histogram bins compared to [10,25,50,100] bins. Subscripts r, i, w and h indicate anhydrous rock, ice, liquid water and hydrous rock respectively.

Number of	Anhydrous rock		Ice		Liquid water		Hydrous rock	
planetesimals	Mass fraction	ϵ_r [%]	Mass fraction	ϵ_i [%]	Mass fraction	ϵ_w [%]	Mass fraction	ϵ_h [%]
5	0.0548	-	0.0940	-	0.505	-	0.346	-
10	0.0525	4.15%	0.0905	3.78%	0.509	0.66%	0.349	0.73%
25	0.0519	5.26%	0.0897	4.64%	0.509	0.80%	0.349	0.92%
50	0.0520	4.96%	0.0900	4.28%	0.509	0.74%	0.349	0.87%
100	0.0519	5.24%	0.0898	4.48%	0.509	0.77%	0.349	0.92%

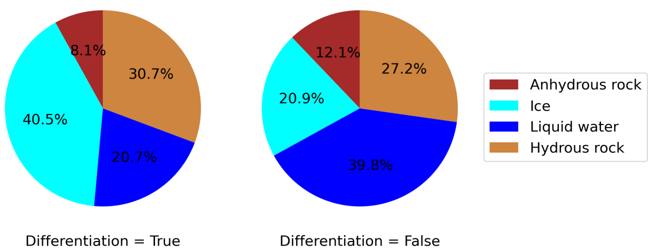

Fig. B.7. Composition of two identical bodies with characteristics shown in Table 7 for layer differentiation settings [True, False].

Appendix C.2: Thermal evolution model integration settings

The effect of varying numerical layer thickness ΔR and integration time Δt on individual planetesimal- and weighted average population composition is shown in Figure C.1 and Figure C.2. For the layer thickness, the pink line indicates the difference between every integration setting and $\Delta R = 0.005 R_p$. The numerical setting chosen is $\Delta R = 0.025 R_p$, where the anhydrous and hydrous rock errors are both below 10%. This choice was made due to computational limitations even though convergence was not yet reached. For the integration time, the error increase w.r.t. $\Delta t = 25$ yr for decreased accuracy is less severe, with an error of 10^{-3}% for $\Delta t = 100$ yr.

Appendix C.3: Differentiation aliasing error

It follows from section 2.3.1 that the boundary between the rocky core and liquid water mantle can not always be approximated by the numerical boundaries (multiples of ΔR), introducing a mass error ϵ_m. Figure C.3 shows both the aliasing error between $R_{\mathrm{r,real}}$ and $R_{\mathrm{r,num}}$ and the altering mass of the planetesimal ϵ_m. The error w.r.t. radius is between the domain $0.5\Delta R$, and ϵ_m between 0.5 M_{layer}. The layer mass M_{layer} increases for layers further away from the core since a constant ΔR spacing is chosen. For a planetesimal with characteristics shown in Table 7, the total mass is 7.1×10^{17} kg and the maximum ϵ_m is 1.6×10^{16} kg (2.3%). The maximum ϵ_m is dependent on ΔR, decreasing for smaller values, as seen by the right panel of Figure C.3.

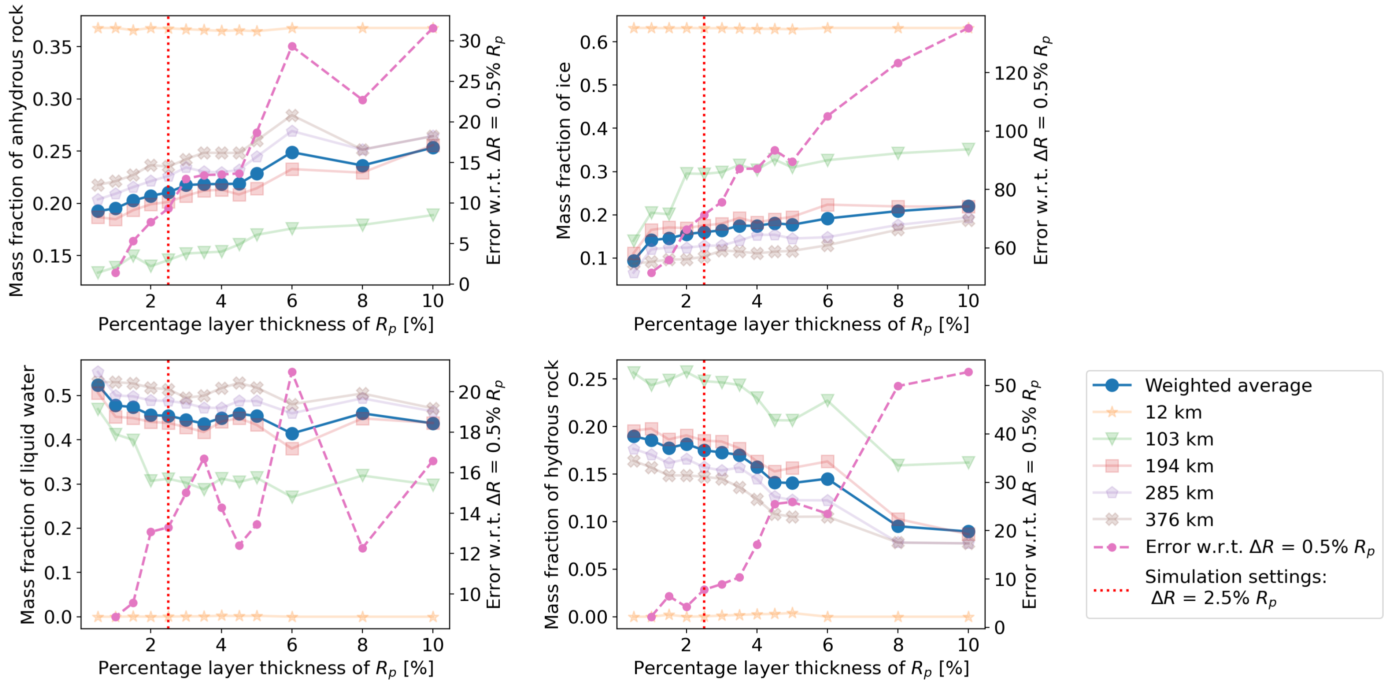

Fig. C.1. Individual planetesimal- and weighted average composition for varying numerical layer thickness ΔR using initial parameters shown in Table 7. The pink line indicates the error w.r.t. $\Delta R = 0.5\%\ R_p$, and the value of $\Delta R = 2.5\%\ R_p$ used in this work is highlighted in red.

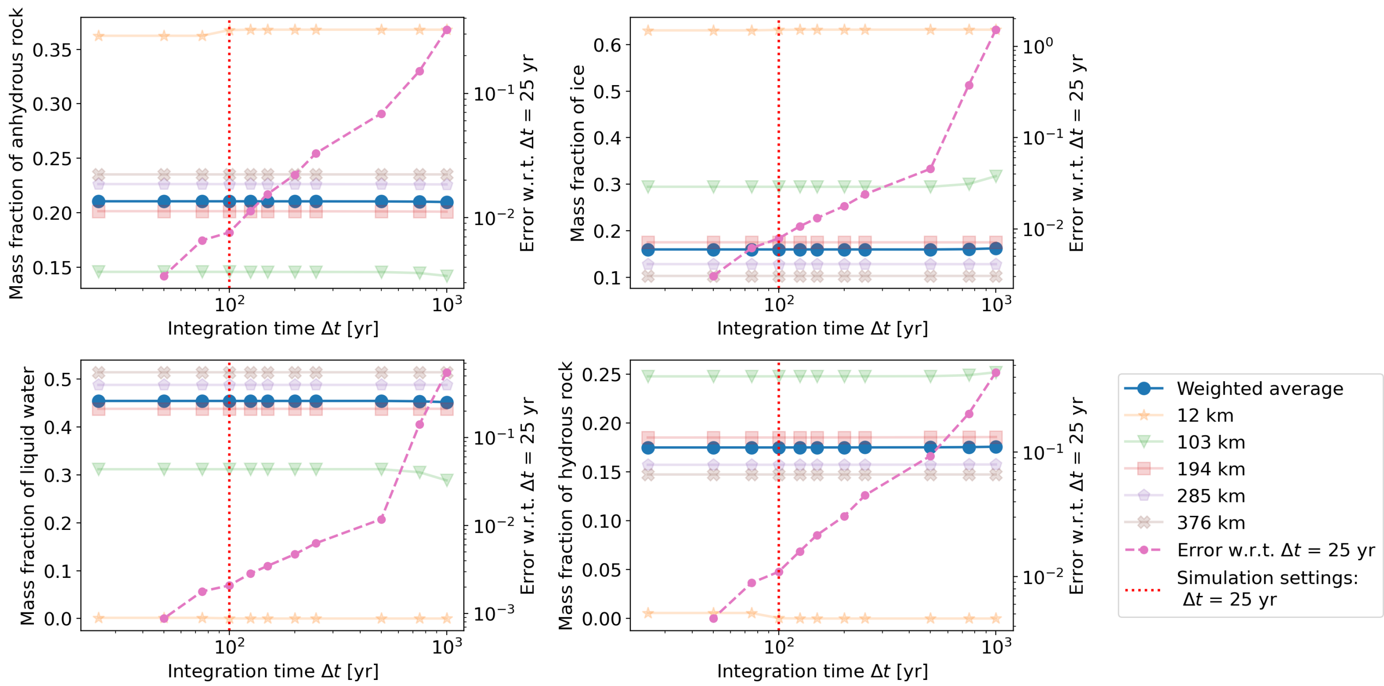

Fig. C.2. Individual planetesimal- and weighted average composition for varying numerical integration time Δt using initial parameters shown in Table 7. The pink line indicates the error w.r.t. $\Delta t = 25$ yr, and the value of $\Delta t = 100$ yr used in this work is highlighted in red.

Appendix C.4: Surface radiation

Variations of ΔR are shown in Figure C.4. For a surface layer thickness of $\Delta R > 2.5\% R_p$, behaviour deviates from the expected surface temperature. The increased layer thickness does not include the second peak around 3 Myr since there are too few layers to support convection from the rocky core to sub-surface layers. This is another reason the thermal evolution model layer thickness ΔR described in section C.2 is set to $2.5\%\ R_p$.

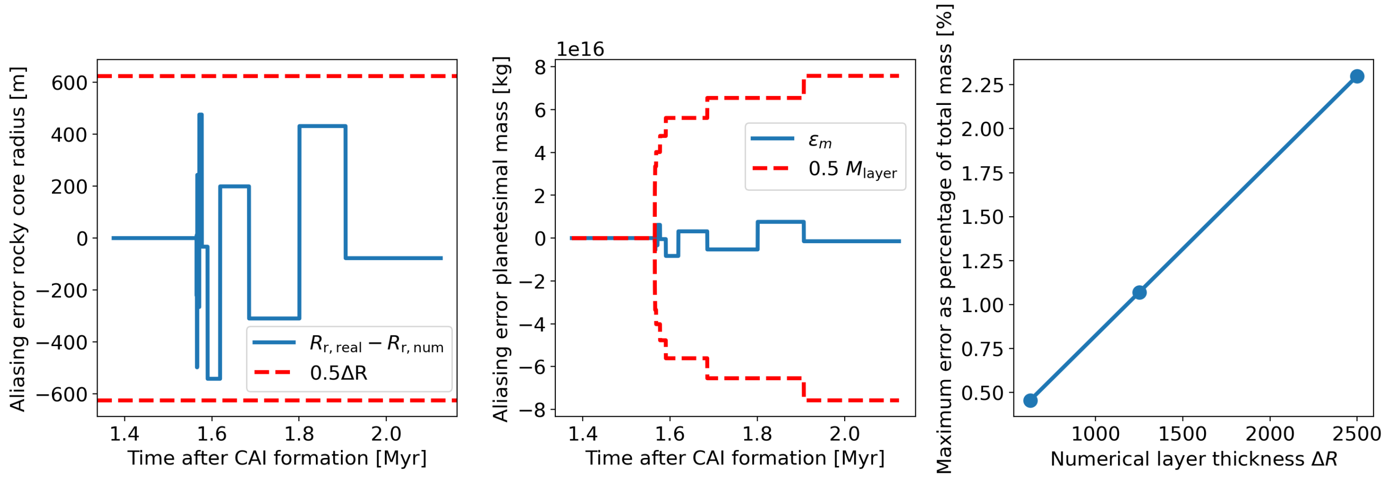

Fig. C.3. The effect of the aliasing error introduced by layer differentiation. Taking a planetesimal with characteristics from Table 7 yields: (Left) The difference between the real differentiation boundary and the numerical boundary which is confined by half the numerical layer thickness. (Middle) The variations in planetesimal mass, confined by half the mass of the layer separating the rocky core and the liquid water mantle. (Right) Dependency of the planetesimal mass error w.r.t. the numerical thickness for [0.05. 0.025. 0.125] ΔR.

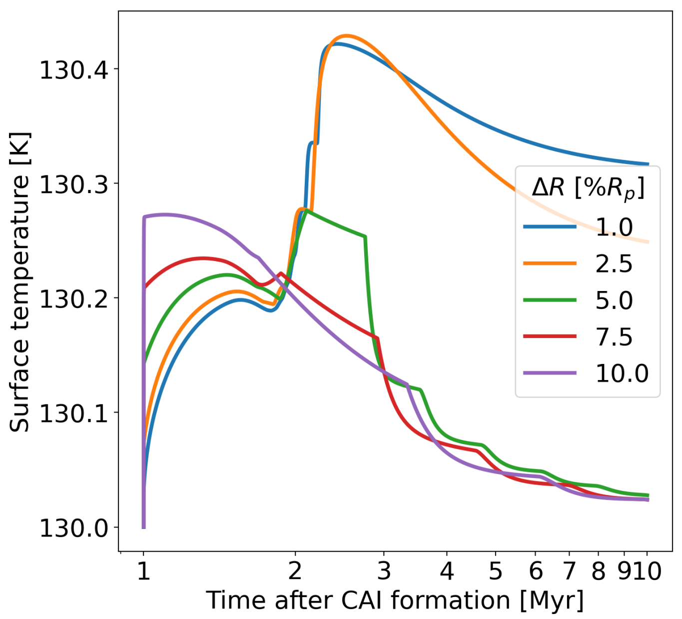

Fig. C.4. Surface temperature for varying layer thickness, presented as percentages of the planetesimal radius [1.0, 2.5, 5.0, 7.5, 10.0] using planetesimal characteristics from Table 7.

3

Verification and Validation

Verification and validation for methods used in the journal article from chapter 2 will be provided in the following sections. The different topics are the streaming instability population generation in section 3.1, the thermal evolution model in section 3.2 and the melting temperature dependence on pressure and ammonia in section 3.3. If equations or tables are referenced from the journal paper, this will be explicitly stated.

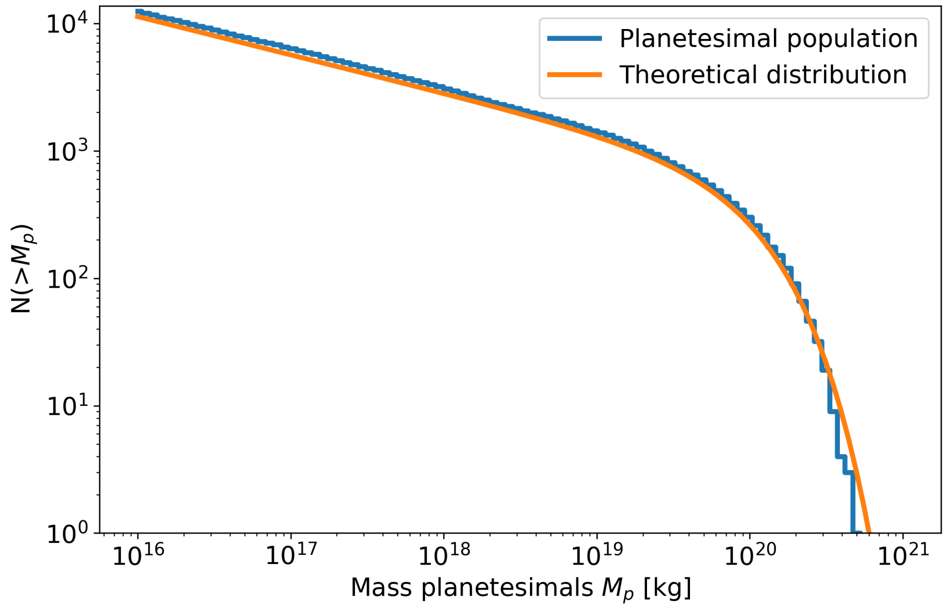

Figure 3.1: Comparison between the sampled distribution and the theoretical curve described by Abod et al. 2019.

3.1. Streaming instability population

In order to check if the planetesimals generated from reversing the resulting from simulations of Abod et al. 2019 is done correctly is shown in Figure 3.1. The resulting population can be seen to follow the theoretical distribution with only slight deviations for the final segment of higher mass planetesimals. The magnitude of $N(> M_p)$ is of the order 1-10 planetesimals and will thus not significantly impact results.

Table 3.1: Comparison of results obtained by thermal model of Wakita and Sekiya 2011 for variations of T_0, R_p and t_{start}, highlighting magnitude of negative and positive outliers by red and blue respectively. Compared parameters are start and stop times of ice melting and dehydration, with "-" indicating condition has not been reached.

$\mathbf{T_0}$ [K]	$\mathbf{R_p}$ [km]	$\mathbf{t}_{start}[Myr]$	$\mathbf{T_{j=0,max}}$ [%]	$\mathbf{t}_{ice,start}$ [%]	$\mathbf{t}_{ice,stop}$ [%]	$\mathbf{t}_{dehydrate,start}$ [%]	$\mathbf{t}_{dehydrate,stop}$ [%]
130	10	0.00	-10.78	-8.91	43.48	-	-
130	10	0.50	-2.79	2.20	16.75	-	-
130	10	1.00	-0.70	-	-	-	-
130	50	1.00	0.55	5.60	11.58	-1.46	3.46
130	50	1.50	2.92	4.54	8.94	-	-
130	50	2.00	0.00	6.50	-	-	-
130	50	2.40	3.09	-	-	-	-
130	100	1.00	-0.33	5.60	10.62	-1.60	9.39
130	100	1.50	5.30	4.54	9.43	-	-
130	100	2.00	0.00	6.49	-	-	-
130	100	2.40	1.21	-	-	-	-
130	500	1.00	-1.31	5.60	6.14	-1.60	0.26
130	500	1.50	6.38	4.54	4.42	-	-
130	500	2.00	0.00	6.49	-	-	-
130	500	2.40	1.22	-	-	-	-
130	1000	1.00	-1.31	5.60	8.73	-1.60	1.17
130	1000	1.50	6.38	4.54	44.70	-	-
130	1000	2.00	0.00	6.49	-	-	-
130	1000	2.40	1.22	-	-	-	-
70	10	0.00	-9.64	-4.76	26.49	-	-
70	10	0.50	-0.01	1.78	1.41	-	-
70	10	1.00	-0.92	-	-	-	-
70	50	1.00	0.00	5.36	10.46	-8.37	-0.96
70	50	1.50	0.46	4.85	3.37	-	-
70	50	2.00	-2.97	-	-	-	-
70	100	1.00	0.00	5.36	16.09	-5.27	5.12
70	100	1.50	6.64	4.85	6.53	-	-
70	100	2.00	-3.53	-	-	-	-
70	500	1.00	0.00	5.36	8.87	-5.27	-
70	500	1.50	6.11	4.85	1.98	-	-
70	500	2.00	-3.49	-	-	-	-
70	1000	1.00	0.00	5.36	13.23	-5.27	-
70	1000	1.50	6.11	4.85	16.95	-	-
70	1000	2.00	-3.49	-	-	-	-

3.2. Thermal evolution model

The thermal evolution model is heavily based on the numerical model of Wakita and Sekiya 2011 along with some proposed additions. For a set of bodies with R_p [10, 50, 100, 500, 1000] km with various formation times t_{start} ranging from [0.0, 0.5, 1.0, 1.5, 2.0, 2.4] Myr after CAI formation, the maximum core temperature, start and finish of ice melting time, start and finish of dehydration reaction are computed and compared with results from Wakita and Sekiya 2011. This has been done for T_0 = 130 K and 70 K in Table 3.1. The additions used in the current model have been turned off to better compare results. Numerical settings were replicated for Δt = 25 yr and choosing a proportional ΔR = $0.01 R_p$. A large outlier is the parameters tied to a planetesimal of R_p = 10 km at very early formation time. For later formation times, this deviation is less. Another strong outlier is T_0 = 130K R_p = 1000 t_{start}. Since this work does not include 0.0 Myr starting times or bodies larger than 400 km, this is an acceptable deviation. In general, melting occurs at later stages given all percentages are positive. For the dehydration reaction, it is for all cases at an earlier stage.

Along with the values presented in Table 3.1, a visual analysis is performed on the core temperature evolution in Wakita and Sekiya 2011, and can be seen in Figure 3.2 for T_0 = 130 K and 70K. Behaviour is identical, with slight variations visible in Table 3.1 for t_{start} = 1.0 Myr. Besides replicating figures and tables, the parameter variations of radius, initial ice fraction and time of formation show similar trends in core temperature.

Some test cases to verify the correct behaviour of the thermal model will now be introduced. The resulting compositions are given in Figure 3.3, where the first two entries are the initial composition and the normal result for the set of initial parameters shown in Table 7 from the journal paper. The test cases are:

- Eliminating all radiogenic heating by setting the fraction of $^{26}Al/^{27}Al$ to zero. Again, this should

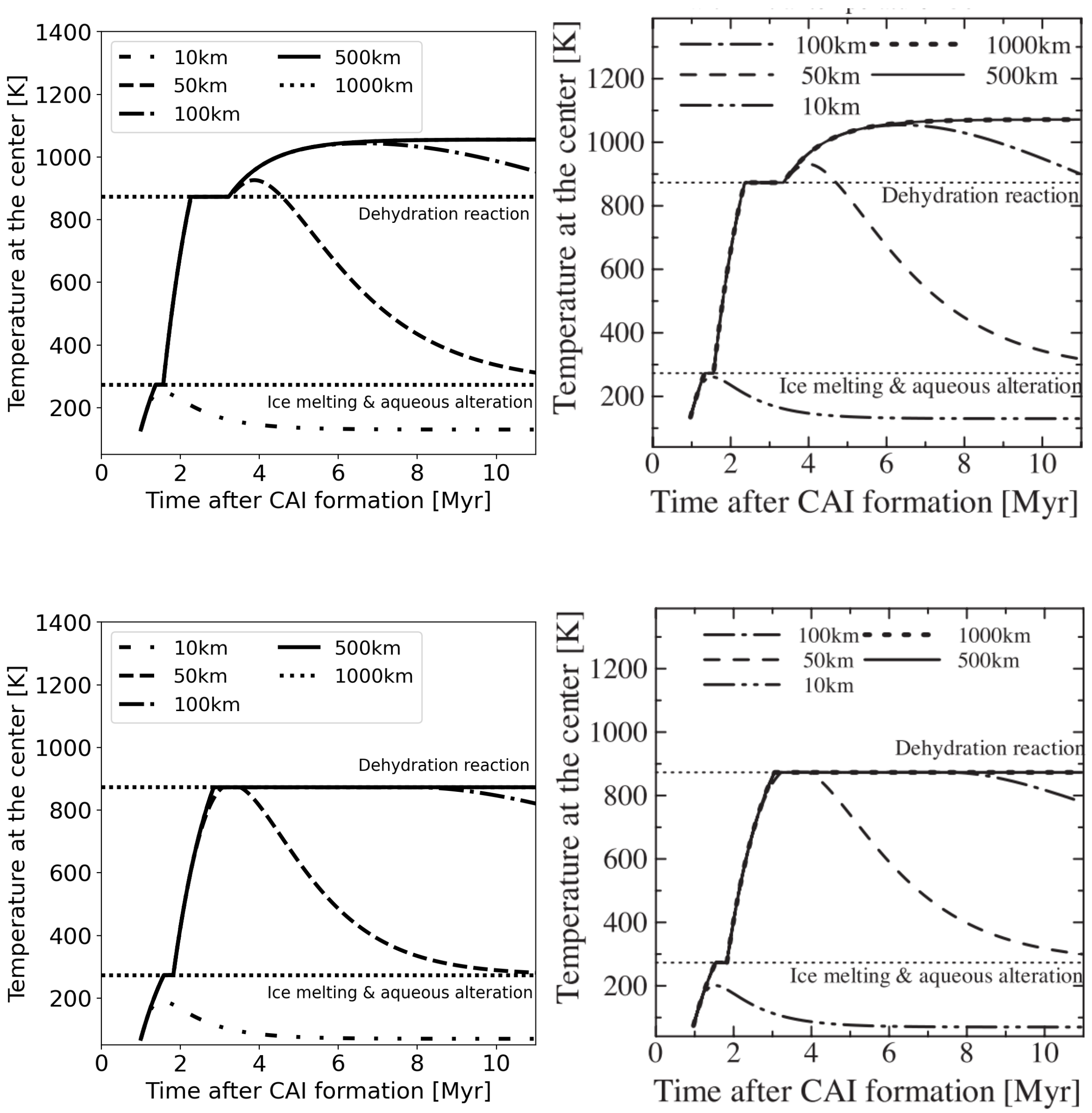

Figure 3.2: Replications of Figure 5 and 6 from Wakita and Sekiya 2011 for (top) T_0 = 130 K and (bottom) T_0 = 70 K. Figures on the (right) have been produced by the numerical model used in this work and (left) are the original images.

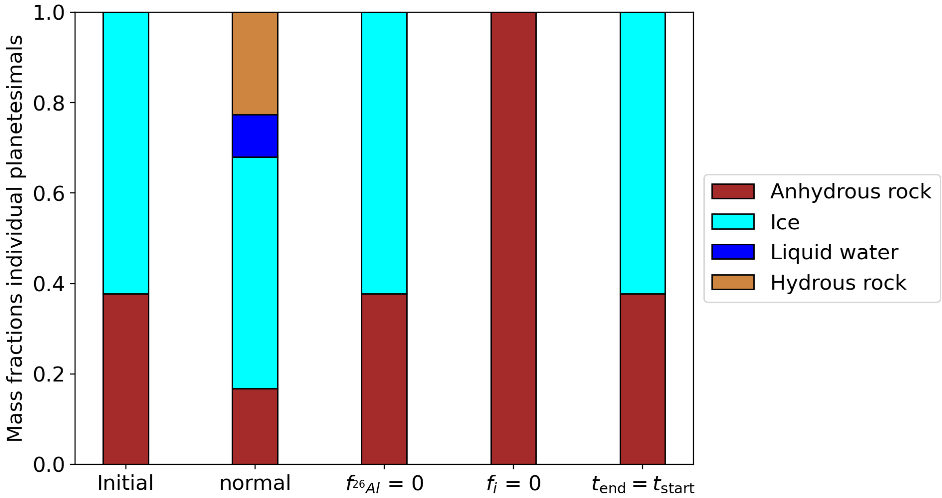

Figure 3.3: Mass fractions of the initial composition, normal thermal evolution with parameters from Table 7 from the journal paper, no radiogenic heating, no ice mass fraction and no integration period.

result in zero heat being generated, thus resulting in the initial composition.

- Reducing the initial ice mass fraction f_i, which should result in no water or hydrous rocks being created. The result should be 100 % hydrous rocks.
- Setting the integration time to 0 Myr, meaning no thermal effects should be able to take place inside the planetesimal. The resulting composition should be the initial composition.

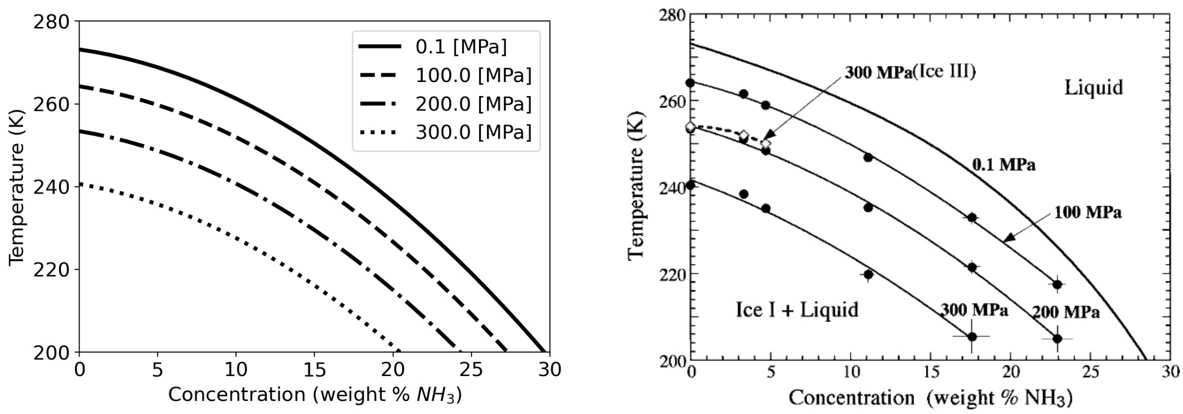

Figure 3.4: A replication of Figure 6 from Leliwa-Kopystyński, Maruyama, and Nakajima 2002 depicting the phase diagram of water-ammonia mixtures on the concentration-temperature plane for pressures [0.1, 100, 200, 300] MPa. (Left) Computations with the model proposed in this work and (Right) the original image.

3.3. Melting temperature dependence on pressure and ammonia

The introduction of a varying melting temperature based on ammonia and internal pressure has to be verified. Seeing if Equation 24 from the journal paper is correctly replicated from Leliwa-Kopystyński, Maruyama, and Nakajima 2002 is shown in Figure 3.4 for pressures [0.1, 100, 200, 300] MPa. Intersections with the y-axis (zero ammonia concentration) line up perfectly, and descending temperature profiles show similar behaviour. Slight alterations come from the assumption of a general formula (Equation 24 from the journal paper) for pressure and concentration from a least-squares fitting of the data points shown in the right image of Figure 3.4. Validating obtained melting pressures is done in Figure 3.5, where the pressure-concentration-temperature space of ammonia is plotted. Since this work only deals with pressures smaller than 200 MPa, only this region of the data from Sotin, Grasset,

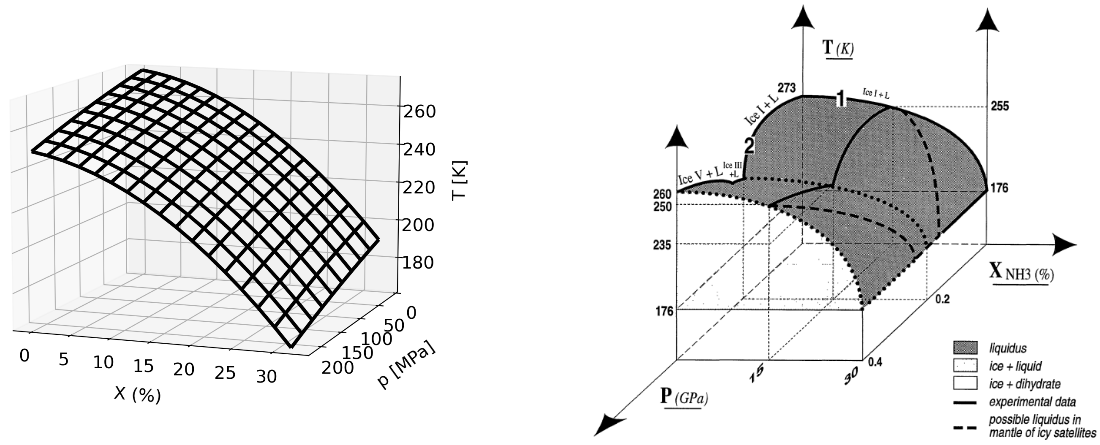

Figure 3.5: Partial replication of Figure 4 of Sotin, Grasset, and Beauchesne 1998 with ammonia concentrations of 0-30%. (Left) Surface plot of the pressure-ammonia concentration-melting temperature regime only reaching a maximum pressure of 200 MPa and (Right) the original image, extending for higher pressures and Ice V and Ice III regions.

and Beauchesne 1998 is replicated. In their work, they assume an isothermal region of 176 K for concentrations of 0.3%, which is not used in this work. The overall shape of the surface plots is similar, decreasing for increased pressure and concentration. Data points that can be compared are P = 0 MPa, $X_{\mathrm{NH_3}}$ = 15%, where the model predicts 250.46 K and 255 K by Sotin, Grasset, and Beauchesne 1998.

Table 3.2: Direct comparison between pressure dependent melting temperatures of the numerical model in this work T_{melt} and values proposed in *Engineering ToolBox* 2017, depicted as the difference in melting temperature ΔT_{melt}.

$\mathbf{P}$ [MPa]	$\mathbf{T}_{\mathrm{melt}}$ [K]	$\Delta\mathbf{T}_{\mathrm{melt}}$ K
0.000612	273.15	-0.01
0.1	273.15	-0.0026
1	273.05	-0.036
2	272.95	-0.06
5	272.75	-0.03
10	272.35	-0.05
15	271.95	-0.06
20	271.55	-0.06
30	270.65	-0.14
40	269.85	-0.09
50	268.95	-0.11
60	268.05	-0.1
70	267.15	-0.06
80	266.15	-0.09
90	265.25	0.01
100	264.25	0.04
120	262.25	0.19
140	260.15	0.35
160	257.95	0.53
180	255.75	0.82
200	253.45	1.13

Excluding the effects of ammonia concentration leaves only the effects of pressure. This will be validated using a data set of different melting temperatures under varying pressures, shown in Table 3.2 (*Engineering ToolBox* 2017). The largest planetesimal in this work does not exceed 400 km, yielding an internal pressure of 64.3 MPa, for which the maximum error occurs at 30 MPa being -0.14 K compared to the validation set. Larger errors are omitted since they only occur for larger pressures of 120 MPa and more.

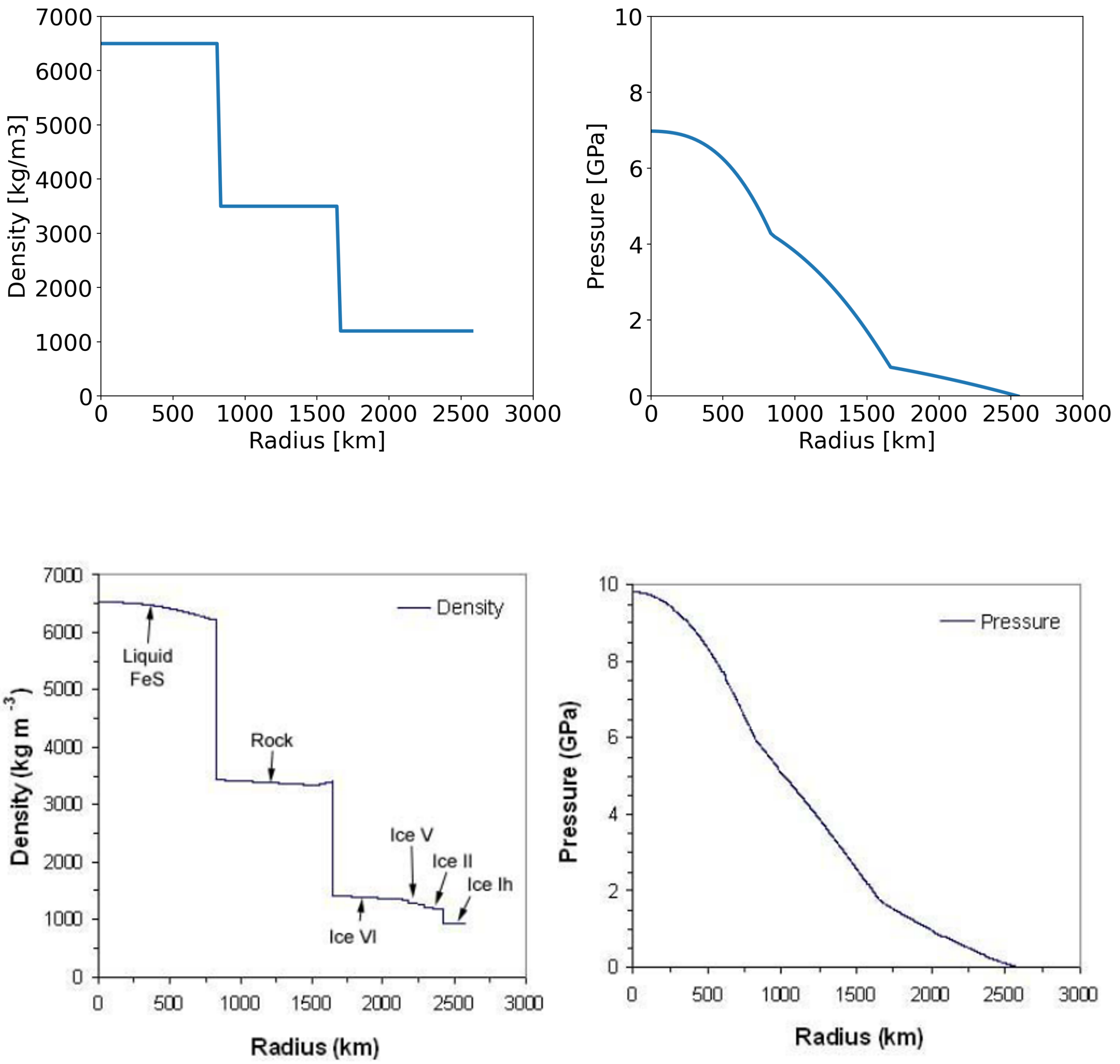

Figure 3.6: Replication of Figure 9.8 from Fortes 2004 for the density and internal pressure of Titan B. Different density layers are estimated at 6500, 3500 and 1000 kg m^{-3}. (Top) pressure computations with own computations (Bottom) original image.

The pressure computations shown in Equation 25 from the journal paper are tested on interior computations of the moon Titan (Fortes 2004). The density profile of the moon is assumed to be [6500, 3500, 1200] kg m^{-3} with boundaries between layers occurring at 820.0 and 164.6 km. This gives a mass difference compared to the validation source of 6.1% with a difference in density of 6.25 %. The pressure diagram and the resulting internal pressure can be seen in Figure 3.6. The total pressure in the core differs by 29.0 %, with the model used in this work having smaller pressures. The pressure profile does, despite the difference in magnitude of the pressure follow the validation source. Titan is more than 5 times larger than the largest objects used in this simulation. According to Toksoz 1974, the moon of Earth has a radius R = 1738 km and mean density of ρ = 3344 kg m^{-3}, giving an internal pressure of 4.6 MPa. When using the numerical model to compute the pressure for the moon, the resulting core temperature is 4.72 MPa, a much closer approximation. For this, a constant density profile is assumed, which is similar to the initial conditions of planetesimals in this work.

4

Conclusions and recommendations

The conclusions and recommendations formulated during this thesis will be listed here. The full methodology along with the results and discussion has been given in the journal article of chapter 2. In short: the radiogenic heating of $^{Al}26$ was analysed for individual but also populations of planetesimals. Temperature profiles and resulting compositions have been analysed. The population of planetesimals has been subjected to conditions of a sample CPD, analysing different parameters and resulting compositions at varying locations in the CPD. Results showed the resulting planetesimal compositions for various parameter variations, composition as a function of radius inside the CPD and the implications of the newly proposed additions of ammonia ice and non-constant surface temperature in the thermal model.

4.1. Conclusions

The research questions posed in chapter 1 can now be answered by the findings of research performed and elaborated upon in chapter 2. This will be done by providing answers to all (sub)questions individually.

1. **How does the total and individual composition of a population of planetesimals change when subjected to internal radiogenic heating?**

   (a) **What are the driving parameters for compositional changes due to radiogenic heating?**

   Temperature evolution inside planetesimals is largely governed by its radius, initial temperature, initial ice and time of formation relative to CAI formation. Large planetesimals that are able to hydrate silicates and show differentiation dominate the weighted average mass fractions in the population. Half of the mass of the planetesimal population is accounted for by bodies with a radius larger than ~250 km. Temperatures are positively correlated with planetesimal radius and initial temperature and negatively correlated with ice mass fraction and formation time, resulting in the formation of hydrous rocks. Temperatures exceeding the dehydration temperature however cause dehydration of previously formed hydrous rock, which is the reason a formation time of 2.0 Myr resulted in the highest amount of hydrous rock (83%). Earlier formation at 1.0 Myr led to more dehydration given the more potent radiogenic heating (73%) and later formation at 3.0 Myr saw the lack of layers reaching the melting temperature (29%).

   (b) **To what extent does ammonia ice affect the compositional changes?**

   With the addition of ammonia ice, the melting temperature of ice was lowered to 198 K for the limit case of X_{NH_3} = 0.3. This significant reduction allows melting of ice for lower quantities of radiogenic heating, decreasing the region in the CPD where hydrous rocks can not be formed from 7.28$\times10^{-2}$ to 7.71$\times10^{-1}$ AU at $t_{start} = 3.0 Myr$. The time it takes for aqueous alteration to occur has lowered from > 2.0 Myr to 1.5 Myr, potentially preventing planetesimal loss due to migration.

(c) **Is there a preferred environment for the creation of hydrous rocks in planetesimals?**
Hydrous rocks are mostly formed in the outer regions of the CPD by the high ammonia concentration in the ice and moderate ice fractions allowing radiogenic rocks to dominate. A local maximum is also found near the ice-line, where temperatures are sufficiently high to counter the higher ice mass fraction and somewhat lower ammonia concentration. The ice mass fraction is essential since it is necessary to form hydrous rocks. Too much ice however means less rock to heat the planetesimal by means of radiogenic heating, pointing towards an optimal between the two explanations.

2. **What are the constraints concerning the formation of the Galilean moons assuming their ice mass fraction was lost by radiogenic heating?**

(a) **At what formation time does ^{26}Al not contribute to the production of hydrous rocks that could serve as building blocks for Europa.**
At a formation time of t_{start} = 4 Myr after CAI formation, the fraction of hydrous rocks created is negligible. This means that for the assumptions posed in this research, the hydrous compounds on Europa can not be formed by radiogenic heating if it is formed at 4 Myr or later. The ratio of ice to rocks to produce hydrous rocks is approximately 1/9. That means that when the hydrous rocks from this research end up becoming a satellite, the conversion of their hydrous rocks might follow this same proportionality. From the 66% hydrous rocks being formed at 3 Myr after 1.5 Myr, a composition of 6.3% ice can be formed after dehydration. Assuming the composition of the planetesimal population ends up in the satellite, the resulting ice mass fraction is in line with the observed low ice mass fraction on Europa of ~5-8%.
It is not expected that Europa formed before Io. If Io also formed 3 Myr after CAI formation, it should have lost its icy composition no later than 1 Myr after the formation of the planetesimals in order to prevent the formation of hydrous rocks.
If differentiation on Ganymede occurred by SLRN heating, it should have formed before 4 Myr. To prevent full differentiation on Callisto, formation should occur after 4 Myr.

(b) **What locations in the CPD around Jupiter can be (de)hydrated by the effects of ^{26}Al.**
For all formation times, the regions where most hydrous rocks are formed are close to Jupiter and at the outer edges of the CPD. This is closely tied to the ice mass fraction, which as described in item 1c seems to be optimal at around 10%, both for the hotter inner- and colder outer parts of the CPD.

4.2. Recommendations

1. The formation time has been analysed on the 1-4 Myr region with an interval of 1 Myr. This gave the result of partial hydration at 3 Myr and no hydration at 4 Myr. To more precisely pinpoint the time no hydration occurs in the CPD will further strengthen the conclusions on the production of hydrous materials for the Galilean system.

2. This research has limited itself to a single planetesimal population formed by the SI assumption and subjected it to the conditions of a single CPD. Different formation theories produce different populations w.r.t. mass distribution and typical planetesimal sizes, which have been shown to alter the resulting composition. This will play a role in analysing satellite systems besides that of Jupiter. Although limited by a single population and CPD, the tools presented in this research can however be adapted for different conditions.

3. The addition of ammonia ice has shown its potential in lowering the melting temperature of ice. In this research, this is the only implication of the introduction of ammonia ice. More details should be introduced to fully simulate the introduction of ammonia ice and its effect on the thermal parameters of conduction, diffusion, specific heat and the resulting density of ice.

4. The surface layer was simulated using three heating sources: internal radiogenic heating, conduction from the sub-surface layer and cooling via surface radiation. The interaction between the surface layer and the surrounding CPD could be modelled in more detail, taking into account the heating of the surrounding gas in the CPD and its ability to cool by moving inside the disk.

5. As of writing this, the proposed launch date of **JU**piter **IC**y moons **E**xplorer (JUICE) is 2023. [1] This spacecraft will perform observations of the moons Ganymede, Callisto and Europa for three years. This will potentially lead to new insights into the formation origin of the Galilean Satellites. Assumptions made in this research should be critically reviewed by new research in the future.

[1] https://https://sci.esa.int/web/juice/

Bibliography

Abod, Charles P. et al. (Oct. 2019). “The Mass and Size Distribution of Planetesimals Formed by the Streaming Instability. II. The Effect of the Radial Gas Pressure Gradient”. In: *The Astrophysical Journal* 883.2, p. 192.

Barr, A. C. and R. M. Canup (Nov. 2008). “Constraints on gas giant satellite formation from the interior states of partially differentiated satellites”. In: *Icarus* 198, pp. 163–177.

Bierson, C. J. and F. Nimmo (July 2020). “Explaining the Galilean satellites’ density gradient by hydrodynamic escape”. In: *The Astrophysical Journal letters* 897.L43.

Bierson, C. J. and G. Steinbrügge (May 2021). “Tidal heating did not dry out Io and Europa”. In: *The Planetary Science Journal* 2.89.

Canup, R. M. and W. R. Ward (Dec. 2002). “Formation of the Galilean satellites: conditions of accretion”. In: *The Astronomical Journal* 124.

Canup, R. M. and W. R. Ward (2009). “Origin of Europa and the Galilean satellites”. In: *Europa*, pp. 59–83.

Castillo-Rogez, Julie C. and J.I. Lunine (2010). “Evolution of Titan’s rocky core constrained by Cassini observations”. In: *Geophysical Research Letters* 37.20.

Engineering ToolBox (2017). *Ice and Water - Melting Points vs. Pressure.* [Accessed 8 March 2022. URL: `https://www.engineeringtoolbox.com/water-melting-temperature-point-pressure-d_2005.html`.

Fortes, A (2004). *Computational and experimental studies of solids in the ammonia-water system*. Doctoral thesis , University of London.

Gillon, Michaël et al. (Feb. 2017). “Seven temperate terrestrial planets around the nearby ultracool dwarf star TRAPPIST-1”. In: *Nature* 542, pp. 456–460.

Gounelle, M. (Sept. 2015). “The abundance of 26Al-rich planetary systems in the Galaxy”. In: *Astronomy&Astrophysics* 582.A26.

Johansen, A. et al. (2014). “Protostars and Planets VI”. In: University of Arizona Press. Chap. The Multifaceted Planetesimal Formation Process, pp. 547–570.

Kargel, Jeffrey S. et al. (2000). “Europa’s Crust and Ocean: Origin, Composition, and the Prospects for Life”. In: *Icarus* 148.1, pp. 226–265.

Leliwa-Kopystyński, Jacek, Minoru Maruyama, and Toshio Nakajima (2002). “The Water–Ammonia Phase Diagram up to 300 MPa: Application to Icy Satellites”. In: *Icarus* 159.2, pp. 518–528.

Lichtenberg, T. et al. (Apr. 2019). “A water budget dichotomy of rocky protoplanets from 26Al-heating”. In: *Nature Astronomy* 3, pp. 307–313.

Lunine, J.I. and D.J. Stevenson (Oct. 1982). “Formation of the Galilean satellites in a gaseous nebula”. In: *Icarus* 52, pp. 14–39.

McKinnon, W.B. (2006). “Formation time of the Galilean satellites from Callisto’s state of partial differentiation”. In: *Lunar and Planetary Science XXXVII* 2444.

Mosqueira, I. and P. R. Estrada (May 2003). “Formation of the regular satellites of giant planets in an extended gaseous nebula I: subnebula model and accretion of satellites”. In: *Icarus* 163, pp. 198–231.

Ogihara, M. and S. Ida (June 2012). “N-body simulations of the satellite formation around giant planets: origin of orbital configuration of the Galilean moons”. In: *The Astrophysical Journal* 753, p. 60.

Ronnet, T., O. Mousis, and P. Vernazza (Aug. 2017). “Pebble Accretion at the Origin of Water in Europa”. In: *The Astrophysical Journal* 845.2.

Schubert, G., J. D. Anderson, et al. (Jan. 2004). “Jupiter. The planet, satellites and magnetosphere.” In: vol. 1. Cambridge University Press. Chap. Interior composition, structure and dynamics of the Galilean satellites, pp. 281–306.

Schubert, G., D. J. Stevenson, and K. Ellsworth (Apr. 1981). “Internal Structure of the Galilean Satellites”. In: *Icarus* 47, pp. 46–59.

Simon, Jacob B. et al. (2016). “The Mass And Size Distribution of Planetesimals Formed By The Streaming Instability. I. The Role of Self-Gravity”. In: *The Astrophysical Journal* 822.1, p. 55.

Sotin, C., O. Grasset, and S. Beauchesne (1998). “Solar System Ices: Based on Reviews Presented at the International Symposium “Solar System Ices” held in Toulouse, France, on March 27–30, 1995”. In: Dordrecht: Springer Netherlands. Chap. Thermodynamic Properties of High Pressure Ices: Implications for the Dynamics and Internal Structure of Large Icy Satellites, pp. 79–96.

Tobie, Gabriel et al. (Feb. 2014). “The origin and evolution of Titan”. In: *Titan: Interior, Surface, Atmosphere, and Space Environment*, pp. 29–62.

Toksoz, M N (1974). “Geophysical Data and the Interior of the Moon”. In: *Annual Review of Earth and Planetary Sciences* 2.1, pp. 151–177.

Urey, H.C. (1955). “The cosmic abundances of potassium, uranium and thorium and the heat balance of the Earth, the Moon and Mars.” In: *Proceedings of the National Academy of Sciences* 41, pp. 127–144.

Wakita, Shigeru and Minoru Sekiya (Aug. 2011). “Thermal evolution of icy planetesimals in the solar nebula”. In: *Earth, Planets and Space* 63.12, pp. 1193–1206.

Wang, Huapei et al. (2017). “Lifetime of the solar nebula constrained by meteorite paleomagnetism”. In: *Science* 355.6325, pp. 623–627.

Weiss, B. P. and W. F. Bottke (June 2021). “What Can Meteorites Tell Us About the Formation of Jupiter?” In: *AGU Advances* 2.2.

Youdin, Andrew N. and Jeremy Goodman (2005). “Streaming Instabilities in Protoplanetary Disks”. In: *Theh Astrophysical Journal* 620.1, pp. 459–469.

Young, E. D. (Feb. 2014). “Inheritance of solar short- and long-lived radionuclides from molecular clouds and the unexceptional nature of the solar system”. In: *Earth and Planetary Science Letters* 392, pp. 16–27.